Thermal and Mechanical Investigations of (Bi,Pb)-2212 superconductor added with different oxide nanoparticles

M. Matar (moustafa.matar@alexu.edu.eg)
Alexandria University
H. Basma
Lebanese University
S. Abbas
Lebanese University
R. Awad
Lebanese University

Article

Keywords: Bi-2212 superconductor, TGA, Vickers microhardness

Posted Date: May 27th, 2022

DOI: https://doi.org/10.21203/rs.3.rs-1642149/v1

Abstract

In this study, superconducting samples of type $Bi_{1.6}Pb_{0.4}Sr_{1.9}Ca_{1.1}Cu_{2.1}O_y$,(Bi, Pb)-2212, added with CdO, CdMnO, and CdFeO nanoparticles, were synthesized using a solid state reaction technique. The samples were examined using X-ray powder diffraction (XRD) and scanning electron microscopy (SEM). Thermogravimetric analysis (TGA) was utilized to evaluate the thermal stability of the pure sample throughout the different stages of the phase formation and the effect of the nanoparticles addition. The weight loss/gain by the three additions is related to the excess of oxygen, confirmed via Iodometric titration analysis and from the findings of oxygen diffusion energy using TGA data. Vickers microhardness measurements were conducted at various applied loads (0.49–9.8 N). All of the prepared samples displayed a typical 'indentation size effect' (ISE) behavior based on the H_V measurements. It was found that the optimum addition of nanoparticles, for increasing the microhardness of the (Bi, Pb)-2212 phase, was at x = 0.05 wt. %. Furthermore, various mechanical properties as Elastic modulus (*E*), yield strength (Y), fracture toughness(*K*), and brittleness index (*B*) were calculated for three additions of the samples studied. As for the theoretical examination of H_V in the saturation limit regions, the indentation-induced cracking (IIC) model wins the comparison.

1. Introduction

From the application point of view, the $(Bi_{2-x}\ Pb_x)Sr_2Ca\ Cu_2O_y$ or (Bi, Pb)-2212 superconducting phase of the $[(Bi_{2-x}\ Pb_x)Sr_2Ca_{n1}CunO_{4+2n+\delta}$, n = 1, 2, and 3] homologous superconducting series is considered one of the most promising phase for further investigations because of its appealing characteristics [1–5]. Similar to the other cuprates, the (Bi, Pb)-2212 is a hard ceramic with numerous small fractures, vacancies, and dislocations. These are found in the $Cu–O_2$ sheets, making them not flexible and moldable due to the absence of yield point and inelastic nature [6]. Therefore, the porous structure and brittle nature are the most problematic quantities for the restriction of using (Bi, Pb)-221 in applications. However, some applications such as magnetic coils, devices for storing magnetic energy, cables of power transmission, etc. [7–10], materials must have adequate mechanical strength, which usually requires precise microstructure control. As a result, the general behavior of mechanical performance and its properties such as Hv, *E*, and *Y* enable materials to be used in their potential application fields and give a broad insight into their microstructure [11].

Vickers hardness is preferred for estimating the mechanical properties of HTSCs due to its inherent benefits, which include non-destructive nature, simple test procedure, low cost, accurate reading, and it is strongly related to their compositions and structures [12]. In this regard, the microhardness measurement results are accurate and valuable in metallurgical, technological, and industrial applications for quality control procedures and materials selection [13]. As a result, many researchers have been working in investigating and improving the mechanical properties as well as structural, electrical, and magnetic properties of HTSCs [14–24], using nano-oxides, nanometals, etc. For example, consider the effect of adding WO_3 (40 nm) to the $Bi_{1.8}Sr_2W_xCa_{1.1}Cu_{2.1}O_y$ superconductor, with x = 0.0, 0.05, 0.1 and 0.25 wt.%,

was studied by Özkurt [25] and demonstrated that extra amount of WO_3 (x = 0.25 wt.%) raised the H_v of the phase. Furthermore, all samples exhibited indentation size effect behavior. In addition, Bahadir Akkurt et al. [26] investigated the effect of replacement of Ca by Gd nanoparticles in Bi-2212 with a nominal composition $Bi_{2.1}Sr_{2.0}Ca_{1.1-x}Gd_xCu_{2.0}O_y$ samples with x = 0.0, 0.01, 0.03, 0.05, 0.07, 0.10, and 0.30. It was found that raising the Gd concentration in the Bi-2212 phase, reduced the mechanical performance and favored the reverse indentation size effect (RISE) behavior. This behavior was explained based on many factors that occur in the samples, such as the coupling problems between the grains, defects, and the plastic deformations that became more prominent with increasing Gd content. In addition, the theoretical modeling showed that the HK model is a good descriptor for defining mechanical properties.

CdO nanoparticles are among the transparent conductive oxide (TCO) nanoparticles that the researchers are interested in because of their beneficial properties [27–29]. The effects of adding CdO nanoparticles to high-temperature superconductors on their superconducting properties have been studied [30, 31]. The structural, optical, and magnetic signatures of the host CdO matrix were found to be improved by transition metal doping, allowing for novel applications. CdO nanoparticles doped with Mn^{2+} [32–34] and Fe^{3+} [35–37] have gotten a lot of attention. Even so, no prior research has looked experimentally at the effect of the addition of $Cd_{0.95}$ $Mn_{0.05}O$ (CdMnO) and $Cd_{0.95}$ $Fe_{0.05}O$ (CdFeO) nanoparticles on the structural, mechanical, and thermal behavior (TGA) of (Bi, Pb)-2212superconducting ceramics. This prompted us to look into the impact of doping (Bi, Pb)-2212 superconducting phase by low concentrations of CdO, CdMnO and CdFeO nanoparticles, having the general formula: $(CdO)_x$ $Bi_{1.6}Pb_{0.4}Sr_{1.9}Ca_{1.1}Cu_{2.1}O_y$ $(Cd_{0.95}$ $Mn_{0.05}O)xBi_{1.6}Pb_{0.4}Sr_{1.9}Ca_{1.1}Cu_{2.1}O_y$ and $(Cd_{0.95}$ $Fe_{0.05}$ $O)x$ $Bi_{1.6}Pb_{0.4}Sr_{1.9}Ca_{1.1}Cu_{2.1}O_y$ with x = 0.00, 0.01%, 0.02%, 0.05% and 0.10% synthesized using the conventional solid-state reaction technique. The aim of this study is to present, for the first time, a comparative study of CdO and its two additives, Mn and Fe, was conducted to investigate the structural, morphological, and thermal behavior (TGA) of the (Bi, Pb)-2212 superconducting phase. In addition, to determine which sample is most desirable for improving mechanical properties. Moreover, theoretical models examination in the saturation limit regions are employed to calculate the true microhardness parameters.

2. Experimental Techniques

A traditional solid-state reaction method was applied to prepare 20 grams powder for each of the superconducting phase of nominal composition: $(CdO)_x$ $Bi_{1.6}Pb_{0.4}Sr_{1.9}Ca_{1.1}Cu_{2.1}O_{y,}$ $(Cd_{0.95}$ $Mn_{0.05}$ $O)xBi_{1.6}Pb_{0.4}Sr_{1.9}Ca_{1.1}Cu_{2.1}O_y$, and $(Cd_{0.95}$ $Fe_{0.05}$ $O)x$ $Bi_{1.6}Pb_{0.4}Sr_{1.9}Ca_{1.1}Cu_{2.1}O_y$ with x = 0.00, 0.01%, 0.02%, 0.05% and 0.10% [38]. Stoichiometric amounts of CuO, Bi_2O_3, CaO, and $SrCO_3$ of high purity were grinded and sieved to obtain a homogenous powder. Afterward, the powders were subjected to thermal treatment as follows. First, the powders were heated at 800 ^oC for 24 h with the aid of a Nabertherm muffle furnace, then they were heated at 820 ^oC for 24 h, with intermediate grinding and sieving. Afterward, the powders were pressed at 0.96 GPa into pellets and sintered at a heating rate of 6°C/min for 50 h at a temperature of 840°C and a cooling rate of 4°C/min. Finally, CdO. $Cd_{0.95}Mn_{0.05}O$, and $Cd_{0.95}Fe_{0.05}O$ nanoparticles of average grain size 41.24 nm, 39.79 nm, and 40.87 nm, respectively.

prepared by the co-precipitation method, as reported in our previous publication [38], were added at the last step, and the mixture was pressed and heated again with a rate of 4 ºC/min at 840 ºC for 48 hours and then cooled at a rate of 2 ºC/min. The X-ray powder diffraction characterization was performed using a Bruker focus diffractometer Cu K_α radiation (λ = 1.5406 Å), with 2θ ranging from 20° to 60°, setting the voltage and the current at 40 kV and 40 mA, respectively. The morphology of the prepared samples was proceeded through a scanning electron microscope (SEM), (JEOL JSM). SEM technique was applied to image the surface with a resolution of 10 µm utilizing an SDD Apollo X with an accelerating voltage of 20 kV and an AIS 2100C microscope operating at 20 kV, respectively. Thermal deterioration and stability were detected by TGA Shimadzu-50H. Each sample was weighed between 5–7 mg, and the weight changes in the samples were sealed in an aluminum pan and monitored in the air while they were heated from room temperature to 900 ^oC at a rate of 10 $^oC\ min^{-1}$. To study the mechanical performance of our samples, the values of HV have been measured at room temperature using a digital microhardness tester (MHVD-1000IS), with a dwell indentation time of 60 sec, and applied loads ranging from 0.49 N up to 9.8 N. The applied loads have been conducted at various parts of the surface samples. To achieve good mean values for each load, an average of five readings at various places on the surface samples were taken.

3. Theoretical Approach

Several investigations [39, 40] have shown that a sample's Vickers microhardness, H_v, is dependent on the static test applied load, F. The following equation is used to compute numerically the Vickers microhardness values for various applied static test loads.

$$H_V = \frac{2Fsin(\alpha/2)}{d^2} = 1854.4\frac{F}{d^2}(GPa)$$

1 ,
where α is the indenter’s face angle of 136°, and d is the adequate mean diagonal length.

Meyer's law is considered a useful model for examining the fundamental mechanical characterization of material under external stress. It predicts one of the two effect, an indentation size effect (ISE) or a reverse indentation size effect (RISE). For ISE a typical decrement in the Vickers microhardness parameters with the applied indentation test loads is observed. For RISE, an unusual increment in the Vickers microhardness parameters with the applied indentation test loads is observed. The following equation can be used to define the behavior of the samples evaluated by Meyer's [41]:

$$F = Ad^n, \quad (2)$$

where A is the constant microhardness value for the material and n is the Meyer number calculated from the fitted curves between LnF and Lnd. This is a crucial value in determining whether a material exhibits *ISE* or *RISE* behavior, if the value of n < 2, ISE nature is observed. In the case of n > 2, RISE behavior is observed.

Based on the elastic recovery mechanism in the vicinity of the indentation track. Elastic/Plastic Deformation (EPD) model is considered a useful one in this range for determining the behavior of the samples (ISE or RISE). When plastic deformation is the dominant feature of the system, the model is much preferable. Because the EPD method emphasizes plastic deformation by adding a new term related to plastic deformation to the theoretical formula as a correlation factor. According to this, the diagonal length on the inside of the plastic deformation, and the elastic/plastic deformation load-independent microhardness (H_{EPDin}) can be calculated using the following relations, respectively [42, 43]:

$$F = A_2 \left(d + d_o\right)^2, \text{and} (3)$$

$$H_{EPDin} = 1854.4 \times A_2. (4)$$

Where A_2 is constant and d_o is indentation size value that is formed with elastic deformation

The mechanical identification of the material exhibiting the *ISE/RISE* nature is described using the proportional specimen resistance (PSR) model for many materials [44]. Moreover, the foundation of the PSR model is the dispersion of energy associated with the occurrence of vacancies, residual cracks, and flaws on the surface sample. The PSR model can be defined using the equations below:

$$F = \alpha d + \beta d^2, \text{and} (5)$$

$$H_{PSRin} = 1854.4 \times \beta. (6)$$

Where α represents the surface energy, β is a parameter that is used to calculate the load-independent microhardness value H_{PSRin}.

Another theoretical approach for examining the mechanical properties of the ceramic is the modified proportional sample resistance (MPSR) model. By comparison with PSR, it was found that the MPSR model incorporates an additional constant given as α_1 for the arrangement of the diagonal length of the indenter on the surface of a specimen. The modified proportional resistance (MPSR) is defined in the literature as [40]:

$$F = \alpha_1 + \alpha_2 d + \alpha_3 d^2, \text{and} (7)$$

$$H_{PSRin} = 1854.4 \times \alpha_3. (8)$$

Where α_1 corresponds to the minimum applied load to produce an indentation, and it is equivalent to the load-independent constant (*W)* in the HK approach. α_1 relates to the surface residual stresses associated with surface polishing and machining. While, the values α_2 and α_3 correspond to the constants α and β in Eq. (5), respectively.

According to the Hays and Kendall (HK) model [45], it was found that there is a critical value of the applied load, W, above which plastic deformation occurs due to the indenter's deep penetration into the sample

[46]. As a result, the effective load, F_{eff} =F-W, is used to formalize the alteration in indentation size against the applied test load instead of the applied load itself, as seen in the following equation:

$$F - W = A_1 d^2, \quad (9)$$

where A_1 is the load-independent microhardness constant

According to HK model, the HK load-independent microhardness (H_{HKin}) is given by the following equation:

$$H_{HKin} = 1854.4 \times A_1. \quad (10)$$

Finally, the last theoretical model discussed in this study is the IIC model, which is used to examine the mechanical performance and true microhardness values in the saturation regions [44, 46]. The IIC model is made up of four primary components that are responsible for the resistance to the imprint diagonal length and particularly determine the behavior of the material (ISE or RISE behaviors): The first two components that cause ISE behavior are the indenter/specimen interface frictional components and elastic deformation, while the second two components responsible for RISE behavior are plastic deformation and crack mechanism. According to the IIC model, the independent load Vickers microhardness is obtained from the following relationship:

$$H_{IIC} = \lambda_1 K_1 (F/d^2) + K_2 (F^{5/3}/d^3)$$

11,

where λ_1 is constant, K_1 is constant rely upon the indenter's geometry, and K_2 is constant depending on the applied load. For type-II superconductors, which are characterized by brittle nature ($\lambda_1 = 0$), thus the above equation is reduced to the following one:

$$H_{IIC} = K \left(\frac{F^{5/3}}{d^3} \right)^m.$$

12

Where K and m are load-independent parameter constants. It is important to note that the m value is similar to the n value in Mayer's law, where both can be used to identify the indentation size effect. The m value has a crucial value of 0.6, if m > 0.6 the material shows ISE behavior, while for m < 0.6 the RISE behavior is exceptional [20].

Additionally, in this study the critical mechanical characteristics regarding the elastic modulus (E), yield strength (Y), and fracture toughness (K) were deduced, which are essential for the use of the Bi-2212 superconducting phase in industrial applications. As a result, the true microhardness values were used to determine the load-independent parameters *E*, *Y*, *K*, and *B* from the following equations:

$$E = 81.9635\mathrm{H_v}$$

13

$$Y = \mathrm{H_v}/3$$

14

$$K = \sqrt{2E\alpha},\ (\alpha,\ surfceenergy)$$

15

$$B = \frac{\mathrm{H_v}}{\mathrm{K}}$$

16

4. Results And Discussion

4.1 X-ray powder diffraction, XRD:

The plots of Fig. 1-a show the room temperature XRD patterns of (Bi, Pb)-2212 superconducting phase added by nano-CdO, nano-CdMnO, and nano-CdFeO for some selected concentrations with x = 0.00, 0.05, and 0.1 wt%. The diffraction peaks with 2θ between 20° and 60° for all three nano additions are well indexed with the tetragonal structure of Bi-2212 space P4/mmm using the JCPDS card No. 00-082-2278 [47]. All XRD spectra demonstrate a single phased Bi-2212 without the detection of impurities. It is believed that the improved crystallinity and purity are attributed to the heat treatment, in specific the prolonged calcination at T = 840 [48]. Moreover, peaks corresponding to CdO, CdMnO, and CdFeO phases were not detected probably because of their low concentrations.

The lattice parameters a, b and c were determined by using a Reitveld refinement on the XRD patterns using the MAUD software [49], and their values are listed in Table 1. While the plots of Figs. 1-b, 1-c, 1-d and 1-e show the refinements of selected concentrations of CdO, CdMnO and CdFeO nanoparticles addition (x = 0.0 and 0.05 wt.%). The values of a show a slight increase with the increase of CdO, CdMnO, and CdMnFeO contents. While the lattice parameters b and c decrease with increasing the addition of CdO, CdMnO, and CdFeO nanoparticles.

The existence of the metal oxide nanoparticle within the Bi2212 phase unit cell may create extra oxygen ions in the BiO layer. This excess oxygen content might induce the relocation of holes from the charge reservoir (BiO layer) to the Cu-O conducting plane [50, 51]. The effect of oxygen content is also reflected on the ratio c/a and the orthorhombic distortion OD ($\frac{\mathrm{b}-\mathrm{a}}{\mathrm{a}}$) which are calculated and presented in Table 1. A reduction of c/a values with the addition of nanoparticles is observed. The ratio c/a is strongly

dependent on the oxygen content of the Bi-2212 superconducting phase. In particular, the excessive oxygen content within the bonds of Cu-O in planes of Cu-O and BiO layers [52–54]. The high oxygen content induces a Jahn-Teller distortion around Cu^{2+} ions, leading to a reduction of the c/a ratio. An increase of OD is demonstrated with the addition of CdO, CdMnO, and CdFeO up to x = 0.02, followed by a decrease. But, all values of OD are less than 1%, approving the stability of the (Bi, Pb)-2212 phase [55].

Figure 2-a depicts the results of the calculated porosity percentage (P %) for all synthesized samples [56]. The figure indicates that the addition of nano-CdO, nano-CdMnO, and nano-CdFeO up to x = 0.05 wt.% minimizes grain porosity and repairs microcracks. Following that, the porosity increases gradually up to x = 0.1 0wt.%. The porosity decreases by 30%, 34% and 39% with x up to 0.05 wt% for (CdO)-Bi2212, (CdMnO)-Bi2212 and (CdFeO)-Bi2212, respectively.

As for the variation of the superconducting transition temperature T_c, dc-electrical resistivity measurements were conducted using the four probe method and are reported elsewhere [57–59]. The results are depicted in the graph of Fig. 2-b. T_c of the (Bi, Pb)-2212 system increases up to x = 0.5 for both CdO and CdMnO nanoparticles addition. Whereas for CdFeO addition T_c increases up to x = 0.02 and then decreases significantly. The enhancement of T_c is attributed to the enhancement of the grain connectivity due to the addition of the nano-oxides. On the other hand, the deterioration of T_c for higher additions of CdFeO and CdMnO might be attributed to the ferromagnetic nature of these oxides. This nature may cancel the supercurrents and terminate the Cu ion long-range coupling in the CuO layers. Similar behavior was observed by Basma et al. [60], for ferromagnetic CoFe2O4 addition on the Gd-123 system.

4.2 SEM measurements:

Figure 3 depicts the SEM microscopy images of (Bi,Pb)-2212 superconductor with selected concentrations of CdO, CdMnO and CdFeO nanoparticles addition (x = 0.00, 0.05 and 0.10 wt.%). The microstructures of the pure sample show large plate-like grains distributed randomly, which is typical for the Bi-based superconductors family [61]. Whereas, the morphology of samples added with x = 0.05 wt.% CdO, CdMnO, and CdFeO nanoparticles show enhanced texturing and growth, most likely due to the added nanoparticles sticking to grain boundaries [62]. In addition, no detection of secondary phases or impurities was observed, in agreement with the XRD results. Moreover, it is obvious that nanoparticle addition increases the microstructure density and reduces the porosity among the grains by up to x = 0.05 wt.% for the three different nano additions to (Bi, Pb)-2212 phase. This observation is supported by the presence of fine inclusions among the (Bi, Pb)-2212 grains. These inclusions correspond to the added nano- CdO, nano- CdMnO, and nano-CdFeO. This leads to enhanced grain connectivity and the filling of voids and cracks [63]. On the other hand, the most porous structure and softest surface are observed in the 0.10 wt.% sample for three nano additions because the platelet grains linked well in the sample are degraded with the addition of the CdO, CdMnO, and CdFeO nanoparticles due to the random orientation and weak links between the grains [64]. This result was found to be consistent with the porosity percentage calculations.

4 – 3 Iodometric Titration-Oxygen content determination

Iodometric titration was employed for the oxygen content determination. The method consists of a two-step redox titration reaction [65,66]. In the first step, the superconductor sample is dissolved in Potassium Iodide (KI) acidic solution to achieve the reduction of copper to copper Iodide (CuI). In a second step, a back titration of the CuI was performed by using sodium thiosulphate ($Na_2S_2O_3$) to determine the oxygen content [67]. The endpoint of titration was detected by using Potassium thiocyanate (KCSN) used as an indicator of idiometry.

The oxygen content, y, in cuprates superconductors might be calculated using the equations below in terms of a parameter H [68].

$$y = 8 + 1.5H; H = \left[\left(V_1 m_2 / V_2 m_1 \right) - 1 \right].$$

17

Where V_1, V_2, m_1, and m_2 are the volumes of $Na_2S_2O_3$ solutions and the sample's masses throughout the titration in the first and the second stages, respectively. An increase of the value of oxygen content with increasing concentrations for three nano additions and their values are listed in Table 1. This behavior indicated that nano-CdO, nano-CdMnO, and nano-CdFeO aid in the addition of more excess oxygen to the pure sample and are compatible with the variation of the lattice parameters discussed in the XRD section. The effective valence of the Cu ions ($Cu^{eff)}$ valence can also be calculated by applying equilibrium between the positive and the negative valence states of the composition elements as shown in Eq. 14, assuming the valency of the elements as (Bi^{3+}, Pb^{2+}, Sr^{2+}, Ca^{2+}, Cd^{2+}, $Fe^{2+}$and O^{2-}):

$$\mathrm{Cu^{eff}} = \frac{2\mathrm{y} - [11.7 + 2\mathrm{x}]}{2}$$

18

.

Where x and y represent the Cd and O contents.

The values of Cu^{eff} are listed in Table 1. The results show an enhancement in the effective valence of Cu for three different nano additions. This enhancement is attributed to the fact that the development of the (Bi, Pb)-2212 phase demands the existence of Cu^{3+} ions in the form of additional oxygen in/or near the CuO_2 planes [69–71]. The excess oxygen atoms increase the Coulomb potential that confines the doped holes in the CuO_2 planes, reducing their total energy [72].

Under the assumption of a homogeneous density of excess oxygen places in the CuO_2 planes, the excess oxygen atoms introduced into the Bi-2212 are found to be turned into a doping distance, d, given as $d = \sqrt{\Sigma}.\, a$. This was accomplished by expressing one doping element's unit area as a square planar arrangement. The excess doping density Σ^{-1}, whose value gives the number of Bi-2212 unit cells per unit area for one oxygen excess atom, is given as Σ^{-1} = ($1-8y^{-1}$) [73]. Moreover, using the formula, $z = \sqrt{(2a)^2 + a^2} = a.\sqrt{5}$, the distance z between any two nearby Cu atoms in a certain direction may

be determined in terms of a parameter. To test the response of nano-CdO, nano-CdMnO, and nano- CdFeO to the pure system, The samples are simply subjected to the above relationships. The values of Σ^{-1}, d, and z are listed in Table 1, and they show that the increasing the concentration of nanoparticles decreases d, while slightly increasing z and Σ^{-1}. This is excellent evidence for raising the hole carrier concentration in the system. This behavior can be explained based on the excess oxygen mechanism in Bi- cuprates as follows: The electrons are transferred from Cu sites to the BiO layer, resulting in the creation of holes on the Cu and electrons on the Bi as $Bi^{3+} + Cu^{2+} \rightarrow Bi^{3-x} + Cu^{2+x}$ [74]. These changes in the Bi valency are due to a change in hole carriers caused by an oxygen excess.

4–4 Thermal analysis

In an attempt to investigate the thermal stability of the pure sample during the phase formation at different temperatures of preparation stages. Moreover, the effect of the addition of CdO, CdMnO, and CdFeO nanoparticles on the phase formation of the (Bi, Pb)-2212 superconducting phase was reported. TGA is a powerful method for examining material's thermal stability by precisely measuring the weight loss/gain of the material while it is heated at a consistent pace. The material's reaction to thermal stress is ascribed to the change in material weight during thermal treatments. This method is ideal for investigating decomposition temperatures in depth and ensuring that material works well within a specified temperature range.

Figures 4-a, 4-b and 4-c show the percentages of the loss of weight and derivative weight as TG-DTG curves for a pure sample at three different calcination temperatures, 800, 820, and 840°C (denoted by P-800, P-820, and P-840, respectively). The pure sample at three calcination temperatures decomposed completely into a series of steps, where each losing weight represented by a step on the TG curve was accompanied by a similar drop on the DTG curve. TGA was used to evaluate the weight loss, indicating that the samples lost weight gradually from above 40°C to around 450°C and 600°C, followed by a gain of weight, and finally a sudden weight loss at around 750°C. While the duration of weight gain for P-840 increased as the temperature increased from 368°C to 750°C. De-oxidation is responsible for steady weight loss, whereas oxidation is responsible for weight gain. The weight loss at 40–450 ◦C is 0.811%, 1.170%, and − 1.281% for P-800, P-820, and P-840, respectively, and might be due to the removal of water adsorbed on the surface of the powder, the decomposition of mixed carbonates, and the crystallization of CaO or Cu_2O [74], which is indicated by the DTG dips at approximately 169°C, 360°C, and 450°C, respectively. The weight gain is 0.6%, 0.65%, and 0.8%, indicating that several transitional phases throughout the formation of (Bi, Pb)-2212 such as Ca_2CuO_3 and CuO begin to form at about 600°C, while crystallization of the $Bi_2Sr_2CuO_y$ phase occurs at the same temperature [75]. Finally, the weight loss is ∼2%, ∼2%and∼1.6% above 750°C, with steep DTG drop at 807.43, 809.45, and 845.8 ^{o}C for P-800, P-820, and P-840 samples, respectively. This is due to the gradual transition of the previously stated phases to Bi-2212 as described by the following equation [76].

$2Bi_2Sr_2CuO_y$+(Sr, Ca) $CuO_2 \rightarrow 2Bi_2Sr_2CaCu_2O_y$. (19)

According to this equation, the formation of Bi-2212 occurs due to the addition of Cu–O and CaO layers into the Bi-2201 phase. As a result, Bi-2201 is more stable in terms of thermodynamics and crystallography than Bi-2212. In general, it may be deduced that at a calcination temperature of 800 ^{o}C, several transitional intermediate phases developed in the calcined powder.

It is observed that the Bi-2201 phase, which forms from CuO and Bi-rich phase and $Bi_2Sr_{3-x}Ca_{1+x}O_7$ phase, are both observable up to 800°C (P-800). While, the mentioned phases completely transform into the final Bi-2212 phase, between 820 (P-820) and 840°C (P-840), hence 840°C is chosen as the sintering temperature to get the best results without any impurities [48].

Figures 5-a and 5-b show the weight loss percentage and derivative weight percentage for the sintered samples of (Bi, Pb)-2212 with the addition of CdO, CdMnO, and CdFeO nanoparticles, with x = 0.05 and 0.10 wt.% for the three nano particles additions. Firstly, by comparing a pure sample calcined at 840 ^{o}C for 50 h (P-840) and after sintering again at the same temperature and time, it was observed that the weight loss before 750°C for P-840°C (≅1.3%) is smaller than the sintered sample (≅1.5%), which means the complete solid-state reaction between the constituent particles occurred to form the (Bi, Pb)-2212 phase which reinforces the purity of the sample. This result is consistent with the XRD patterns in Fig. 1, which showed that all XRD spectra demonstrate a single phased Bi-2212 without the detection of impurities. It is believed that the improved crystallinity and purity are attributed to the heat treatment, in specific the prolonged calcination at T = 840. Secondly, despite the presence of several dopants of different nanoparticles, the TG-DTG curves behave in the same manner for the growing process. It can be inferred from Fig. 5a, that all the samples decomposed completely in a series of steps. The curves revealed that after the initial weight loss of water, large and small dips in the DTG curve (Fig. 5b) occurred in all the samples. Based on the behavior of oxygen out/diffusion, the weight loss/gain with temperature can be explained by TGA analysis. As we know, the B-2212 superconducting phase comprises oxygen deficits in its unit cell. Thus, to develop the superconductivity of Bi-2212, its unit cell must be filled with oxygen ions. The oxygen diffusion activation energy, E, may be computed using the following formula [77]:

$$ln\left[ln\left(\frac{m}{m_o}\right)\right] = -\frac{E}{R}\left(\frac{1}{T}\right) + constant,$$

18

where m and m_o are the masses of the samples at a given temperature and the samples' beginning mass, respectively, and R is the ideal gas constant. The plots of $\ln[\ln(m/m_o)]$ vs 1/T are depicted in Fig. 5c, for three different nano particles additions with x = 0.00, 0.05, and 0.10 wt.%, where the oxygen diffusion activation energy is calculated from the slope of the lines and are listed in Table 2. E was estimated for $T \geq$ 750 ^{o}C to be 5.508 kJmol^{-1} for the pure sample and then increased with increased nano-CdO to be 8.080 kJmol^{-1} (0.05 wt.%) and 8.466 kJmol^{-1} (0.10 wt.%). While for nano-CdMnO it was 9.798 kJmol^{-1} (0.05 wt.%) and 11.729 kJmol^{-1} (0.10 wt.%). The E values for nano-CdFeO are7.007 kJmol^{-1} (0.05 wt.%) and 9.749 kJmol^{-1} (0.10 wt.%). The high activation energy for diffusion indicates that the fast rate of

diffusion of oxygen into the Bi-2212 phase occurs to compensate for the deficiency in oxygen. Hence, as the addition of nanoparticles increases, the amount of oxygen deficiency decreases and the diffusion is dependent on oxygen content [78]. This dependence was confirmed by the plots as a deviation from straight lines; because the observed dependence is an increase in the value of the activation energy with oxygen content. The plots would curve downwards to slower values (an increase in the slope of the lines) as temperature decreased. The curves of weight change show a fast variation, which supports the increase in activation energy [79].

4–5 Vickers microhardness measurements

Using Vickers microhardness measurements, this study reveals a clear correlation between major changes in general mechanical features and mechanical characteristic behaviors of $Bi_{1.6}Pb_{0.4}Sr_{1.9}Ca_{1.1}Cu_{2.1}O_y$ superconducting phase with the addition of $(CdO)_x$, $(CdMnO)_x$, and $(CdFeO)_x$ nanoparticles in the crystal structure. In this regard., firstly, the discussion of the influence of the adding mechanism on the changes in the values of Vickers hardness (H_V). Figure 6 illustrates graphically the changes in H_V against the applied test load F using Eq. (1) for selected concentrations with x = 0.0,0.01, 0.05, and 0.1 wt.% for the three nano particles additions. According to the results of experimental measurement, it is easy to conclude that, increasing the $(CdO)_x$, $(CdMnO)_x$, and $(CdFeO)_x$ in the Bi-2212 phase causes a significant variation in H_v values. Evidently, for three different nanoparticles additions, the increase of addition up to x = 0.05 improves the H_v values significantly, after which the H_v decreases at x = 0.10 wt. %. Therefore, the optimum doping impurity (x = 0.05 wt.%) for three nano additions results in structural improvements, and the H_V of the (Bi, Pb)-2212 phase is increased significantly by the addition of $(CdO)_x$, $(CdMnO)_x$, and $(CdFeO)_x$ nanoparticles.

This improvement can be attributed to the reduction in porosity or resistance to crack propagation among the grains as well as the enhancement of grain connectivity by adding nanoparticles up to 0.05 wt% into the (Bi, Pb)-2212 phase. While, H_V reduction for x = 0.10 wt% could be due to a variety of factors including increased grain boundary weak links, specimen cracking/porosity, disorder, and irregular grain orientation distribution [47]. These results are consistent with the results observed from SEM micrographs and the porosity calculations. Another interesting result seen in Fig. 6 is that, the H_V parameters values for $(CdO)_x$(Bi,Pb)-2212, $(CdMnO)_x$(Bi,Pb)-2212 and$(CdFeO)_x$(Bi,Pb)-2212 at a static load 0.49 N are found to be within 1.777–1.291, 1.956–1.396 and 2.066–1.573 GpPa, respectively, while at a static load 9.80 N they are to 0.592 − 0.388, 0.632 − 0.408 and 0.686 − 0.481, respectively. In this respect, the bulk $(CdFeO)_x$(Bi, Pb)-2212 phase demonstrates the highest key mechanical design features, thus the CdFeO nanoparticles have the greatest enhancement on the Vicker hardness values Hv for the (Bi, Pb)-2212 phase. Moreover. Table 4 shows that the addition of 0.05 wt.% of CdO, CdMnO and CdFeO enhanced the load-independent H_V by 77.38%, 104.13%, and 113.83%, respectively. Additionally, the enhancement caused by CdFeO is 20.44% and 4.75% as compared to the two additives, CdO and CdMn, respectively. For now, the Hv values decrease consistently up to an applied load of 2.94 N, and the hardness parameters values nearly remain constant above this applied load value, as can be shown in Fig. 6. The value of 2.94

N might thus be considered the saturation limit region. Meaning that the samples in the entire doping range exhibit the typical ISE nature (simultaneous elastic and plastic deformations in the material due to recovery of the system), as explained based on the indenter penetration depth [80,81]. These results are supported by the values of Meyer's number n (Table.3) ($n < 2$, for all samples) obtained from the fitted curves of the experimental data between ln *F* versus ln *d* as shown in Fig. 7. According to Table 3, all of the prepared samples are considered hard materials because the values of n are between 1 and 1.6 ($1 < n < 1.6$) [82,83]. which confirms the high-temperature superconductor's ceramic behavior.

According to the EPD model, Fig. 8 depicts the variation of $F^{0.5}$ against *d* for the (Bi, Pb)-2212 phase added by nano-CdO, nano-CdMnO, and nano-CdFeO, with x = 0.00, 0.05, and 0.10 wt.%. The values of A_2 and d_o are listed in Table 3. The calculated values of d_o are positive with a decrement trend in their values with the enhancement of the addition level to x = 0.05 wt.% for three nano additions. This statement confirms that elastic as well as plastic deformations occur side by side for all our samples [84], confirming that, the addition of CdO, CdMnO, and CdFeO into the (Bi, Pb)-2212 crystal enhanced the mechanical features. The reduction in A_2 at x = 0.10 wt. % is due to an increase in disorders and weak links between the grains, which results in a reduction in observed microhardness and fast crack propagation [20]. Table 4 shows each H_{EPDin} value for each sample of the three different nanoparticles additions to (Bi,Pb)-2212 phase. Due to the far expectation values, it is logical to conclude that this model is insufficient to define the original load-independent values for all prepared samples of the three nano additions to (Bi,Pb)-2212 phase in the saturation region.

The variation of *F/d* against *d* for each phase (x = 0.00, 0.05, and 0.10 wt.%) is pictured in Fig. 9 using the PSR model. Table 3 lists all of the extrapolated parameters (α and β) from the graph. According to Table 3, every sample exhibits the standard ISE feature due to the positive values of the α parameter, confirming the immediate production of both elastic and plastic deformations. While, the *β* parameter is found to have a similar variation trend as H_V with x for three nano additions, confirming the enhancement of grain connectivity and local structure between the grains. Furthermore, the H_{PSRin} values are lower than the measured load-independent microhardness values in the saturation regions. This means the PSR model is not practically sufficient to determine the load-independent values., H_V, and is considered the worst theoretical model among the other theoretical models applied to nano-CdO, nano-CdMnO, and nano-CdFeO/(Bi, Pb)-2212 superconducting samples

Variations of *F against d* are depicted in Fig. 10, and the obtained fitting parameters of the MPSR model (α_1, α_2, and α_3) are listed in Table 3. Two major conclusions are drawn from the values of α_3 parameters: Because of the positive $\alpha_3$values, the samples have an ISE nature, and the ISE characteristic tends to grow systematically with the addition of CdO, CdMnO, and CdFeO nanoparticles until the value of x = 0.05 wt.%. Table 4 shows the calculated values of the load-independent microhardness H_{MPSRin}. It's easy to notice that the MPSR approach's Vickers hardness, H_{MPSRin}, findings are substantially lower than the experimental microhardness values in the plateau region. As a result, this model is ineffective in computing the original load-independent values.

The linear plotting of F versus d^2 is given in Fig. 11 for the (Bi,Pb)-2212, added by CdO, CdMnO and CdFeO nanoparticles,with x = 0.00, 0.05 and0.10 wt.%. Table 3 shows the values of the HK approach's fitting parameters (A_1 and W). It is visible from the table that the W values are positive in each of the three nanoparticles additions showing the *ISE* nature. indicating that under the applied indentation test load, every sample has both elastic and plastic deformations. Moreover, all of the load-independent microhardness H_{HKin} values (Table 4) for three phases are observed to be close to the values of the Vickers hardness in the saturation region. But at the same time, they are far from the values of the IIC model in the saturation regions with respect to the values of the Vickers hardness in the saturation region. Hence, the HK model is inadequate for determining the initial microhardness values for the samples prepared for this study.

According to IIC, the values of K and m parameters are calculated from the variation of ln (Hv) versus indentation test load, ln($F^{5/3}/d^3$) curves as depicted in Fig. 12. All the calculation results are represented in Table 3 in detail, which show that all the values of m for all the samples are higher than the crucial value of 0.6, i.e., m > 0.6. These findings show that all our samples exhibit ISE behavior and are consistent with the findings from Meyer's law. Moreover, Table 4, reveals that H_{IICin} microhardness values are much closer to the load-independent microhardness values in the plateau region in comparison to the other approximation models in this study. As a result, the IIC is an adequate methodology for the mechanical identification of nano-CdO, nano-CdMnO, and nano-CdFeO added to Bi-2212, according to the shreds of evidence produced using this method.

Moreover, there is a link between H_V and the mechanical parameters E, Y, K, and B, which mention the elastic deformation ability of a material when subjected to a force, the point of transition between elastic and plastic deformation, and, very crucially, from the viewpoint of an industrial application, the material's capacity to withstand cracks, propagation, and fracture. The values of E, Y, K, and B for three nano additions can be calculated using (13), (14), (15), and (16), respectively, and their values are represented in Table 4. For three phases, Table 4 shows that E, Y, K, and B rise consistently as x increases up to 0.05 wt.% before displaying a substantial decline at x = 0.10%. where the increase in their values can be explained based on the occupation of nanoparticle inter-grains and voids of the (Bi, Pb)-2212 phase [16]. However, the optimum added concentrations of CdO, CdMnO, and CdFeO nanoparticles in three phases should not exceed 0.05 wt.%, respectively, to obtain a maximal increase in the mechanical characteristics of the (Bi, Pb)-2212 phase. Moreover, CdFeO addition outperformed CdO and CdMnO addition in improving the parameters of E, Y, K, and B, which display better ductility and an enhanced capacity to resist indentation fractures.

Conclusion

The effect of nano-CdO, nano-CdMnO, and nano-CdFeO additions on the phase formation, microstructure, thermal stability (TGA), and mechanical characteristics of (Bi, Pb)-2212 superconducting phase was studied. The formation of (Bi, Pb)-2212 completely occurred at a temperature of 840 ^oC, where above it there is thermal stability as shown by TGA analysis. The weight loss/gain by the addition of CdO, CdMnO, and CdFeO nanoparticles was related to the excess of oxygen calculated through Iodometric titration

analysis. The high values of oxygen diffusion activation energy estimated by TGA analysis show that oxygen deficits were reduced throughout the formation of (Bi, Pb)-2212 superconducting phase confirming the high stability of the samples and consistency with XRD findings. Microhardness values of (Bi, Pb)-2212 added by nano-CdO, nano-CdMnO, and nano-CdFeO were found to increase gradually up to x = 0.05 wt.%, verifying the strengthening of the grain-to-grain linkages. CdFeO addition outperformed CdO and CdMnO addition in improving H_V in the plateau region, with an enhancement of 113.83%, 20.44%, and 4.75% as compared to the pure sample and its two additives, CdO and CdMn, respectively. In the prepared samples, normal ISE behavior was found since H_V dropped as the applied load increased. Six theoretical models explored in this extensive study are effective in mechanical modeling of the acquired H_V values, allowing us to detect the influence of the addition process of nanoparticles on the mechanical features and stability in the (Bi, Pb)-2212 phase. when the results of the models are compared, the IIC model provided considerably closer findings in terms of load-independent microhardness. In addition, the mechanical parameters E, Y, K, and B for three nanoparticle additions appeared to follow the same pattern as the variation of H_V values with the content of nanoparticle additions.

Declarations

Acknowledgments:

This research was accomplished in the Specialized Materials Science Lab and Advanced Nanomaterials Research Lab, Physics Department, Faculty of Science, Beirut Arab University, Lebanon, in cooperation with the superconductivity and metallic-glass lab, Faculty of Science, Alexandria University, Egypt.

References

1. AT, S., EP, A. & Mani, A. Evolution of Superconducting Properties of Coexistent Bi-2212 and Bi-2223 phases in BSCCO. Indian Journal of Pure & Applied Physics (IJPAP), **59**(5), 391-397 (2021).
2. Watanabe, T., Nakagawa, K., Sugimoto, C., Takano, K., Ito, R., Kawamata, T. & Kato, M. Synthesis of the Ba-substituted Bi-2212 phase of BiPb $(Sr, Ba)_2$ $RECu_2O_8$. Japanese Journal of Applied Physics, **59**(5), 050902 (2020).
3. Labban, W., Malaeb, W., Habanjar, K., Hassan, M.S, Sakagami, R., Kamihara, Y. & Awad, R. Investigations of arsenic substitution on the physical, electrical and magnetic properties of Bi-2212 superconductors. Phase Transit. **93,** 1055–66 (2020).
4. Belala, K., Galluzzi, A., Mosbah, M.F.& Polichetti, M. Transport and magnetic properties of Bi (Pb) 2212 superconducting ceramics doped by low rate of potassium. Mater. Sci. -Pol **39,** 15–23 (2021).
5. Koblischka, M. R., Koblischka-Veneva, A., Zeng, X., Hannachi, E. & Slimani, Y. Microstructure and fluctuation-induced conductivity analysis of $Bi_2Sr_2CaCu_2O_{8+\delta}$ (Bi-2212) nanowire fabrics. Crystals, **10**(11), 986 1-17 (2020).
6. Sheahen, T.P. Introduction to High-Temperature Superconductivity, 1st ed^n. (Kluwer Academic Publishers, New York, 2002).

7. Koyama, K., Kanno, S. & Noguchi, S. Electrical, magnetic and superconducting properties of the quenched $Bi_2Sr_2Ca_{1-X}Nd_XCu_2O_{8+y}$ system. Jpn. J. Appl. Phys. **29**, L53–L56 (1990).
8. Ulgen, A.T., Turgay, T., Terzioglu, C., Yildirim, G. & Oz, M. Role of Bi/ Tm substitution in Bi-2212 system on crystal structure quality, pair wave function and polaronic states. J. Alloys Compd. **764**, 755–766 (2018).
9. Guner, S.B., Zalaoglu, Y., Turgay, T., Ozyurt, O., Ulgen, A.T., Dogruer, M. & Yildirim, G. A detailed research for determination of Bi/Ga partial substitution effect in Bi-2212 superconducting matrix on crucial characteristic features. J. Alloy. Compd. **772,** 388–398 (2019).
10. Miao, H., Meinesz, M., Czabai, B., Parrell, J. & Hong, S. Microstructure and Jc improvements in multiflamentary Bi-2212/Ag wires for high field magnet applications. AIP Conf. Proc. **986**, 423–430 (2008).
11. Saritekin, N. K., Terzioglu, C., Pakdil, M., Turgay, T. & Yildirim, G. Solubility limit of tetravalent Zr nanoparticles in Bi-2223 crystal lattice and evaluation of fundamental characteristic properties of new system. J. Mater. Sci.: Mater. Electron **27**, 1854–1865 (2016).
12. Kahraman, F. Evaluation of the Vickers microhardness and fracture toughness on hot pressed Bi-2212/Ag ceramic composites. J. Mater. Sci.: Mater. Electron. **27,** 8006–8012 (2016).
13. Asikuzun, E., Ozturk, O., Cetinkara, H.A., Yildirim, G., Varilci, A., Yılmazlar, M. & Terzioglu, C. Vickers hardness measurements and some physical properties of Pr_2O_3 doped Bi-2212 superconductors. J. Mater. Sci.: Mater. Electron. **23**, 1001–1010 (2012).
14. Zalaoglu, Y., Karaboga, F., Terzioglu, C. & Yildirim, G. Improvement of mechanical performances and characteristics of bulk Bi-2212 materials exposed to Au diffusion and stabilization of durable tetragonal phase by Au. Ceram. Int. **43**,6836–6844 (2017).
15. Abdeen, W., Marahba, S., Awad, R., Abou Aly, A.I, Ibrahim, I.H.& Matar, M. Electrical and mechanical properties of (Bi,Pb)-2223 substituted by holmium. J. Adv. Ceram. **5,** 54–69(2016).
16. Cavdar, S., Deniz, E., Koralay, H., Ozturk, O., Erdem, M. & Gunen, A. The effect of PbSe addition on the mechanical properties of Bi-2212 superconductors. J. Supercond. Novel Magn. **25**, 2297–2307 (2012).
17. Zalaoglu, Y., Bekiroglu, E., Dogruer, M., Yildirim, G., Ozturk, O. & Terzioglu, C. Comparative study on mechanical properties of undoped and Ce-doped Bi-2212 superconductors. J.Mater. Sci.: Mater. Electron. **24,** 2339–2345 (2013).
18. Turgay, T. & Yildirim, G. Effect of aliovalent Si/Bi partial substitution on propagation mechanisms of cracking and dislocation in Bi-2212 crystal system. J. Mater. Sci: Mater. Electron. **30**, 7314–7323 (2019).
19. Habanjar, K., El Haj Hassan, F. & Awad, R. Effect of $BaFe_{12}O_{19}$ nanoparticles addition on (Bi,Pb)-2223 superconducting phase. Mod. Appl. Sci. **13**, 61–71 (2019).
20. AbuHlaiwa, H., Basma, H., Rekaby, M. & Awad, R. Influence of lead fluoride on the mechanical properties of $(Cu_{0.5}Tl_{0.5})$:1223 Phase. Applied Physics A 125:**715** 1-10 (2019).

21. Rmeid, S., Basma, H., Roumie, M., Elhaj Hassan, F. & Awad, R. Vickers Microhardness Studies for $SmBa_2Cu_3O_{7-\delta}$ Added with NiO Nanosized Particles. Journal of Superconductivity and Novel Magnetism **32** (10), 3037-3046 (2019).
22. Barakat, M.M., Abou-Aly, A.I., Awad, R., Aly, N.S. & Ibrahim, S. Mechanical properties of $Y_{3-x}Nd_xBa_{5-x}Ca_xCu_8O_{18-\delta}$ samples. J. Alloy. Compd., **652,** 158–166 (2015).
23. Awad, R., Abou Aly, A.I., Mohammed, N.H., Isber, S., Motaweh, H.A. & El-Said Bakeer, D. Investigation on superconducting properties of $GdBa_2Cu_3O_{7-\delta}$ added with nanosized $ZnFe_2O_4$. J. Alloy. Compd., **610,** 614–622 (2014).
24. Anas, M., Ebrahim, S., Eldeen, I.G., Awad, R. & Abou-Aly, A.I. Effect of single and multi-wall carbon nanotubes on the mechanical properties of Gd-123 superconducting phase, Chem. Phys. Lett., **686**, 34–43 (2017).
25. Özkurt, B. The influence of WO_3 nano-particle addition on the structural and mechanical properties of Bi1.8Sr2Ca1.1Cu2.1Oy ceramics, J. Mater. Sci.: Mater. Electron. **24,** 4233–4239 (2013).
26. Akkurt, B. &Yildirim, G. Change of mechanical performance and characterization with replacement of Ca by Gd nanoparticles in Bi-2212 system and suppression of durable tetragonal phase by Gd. J. Mater. Sci.: Mater Electron **27**, 13034–13043 (2016).
27. Khalaf, A., Matar, M. & Abdeen, W. Tunable Band Gap and Antiferromagnetic Ordering in Co Doped CdO Nanostructures. Journal of Superconductivity and Novel Magnetism **34**, 2911–2921 (2021).
28. Dakhel, A. A. Generation of Magnetic Properties in Degenerated Ni and Ga Codoped CdO Nanocrystals.J Supercond Nov Magn **33,** 1871–1877(2020).
29. Upadhyay, G.K., Kumar, V.& Purohit, L.P. Optimized CdO:TiO_2 nanocomposites for heterojunction solar cell applications. J. Alloys Compd. 1-6 (2021).
30. Ghahfarokhi, S. M., Hoseenzadeh, N. & Shoushtari, M. Z. The Effect of CdO Nanoparticles on the Structure and Magnetic Properties of $Bi_{1.64}Pb_{0.36}Sr_2Ca_{2-x}Cd_xCu_3O_y$. Superconductors. Journal of Superconductivity and Novel Magnetism **27**(10), 2217-2223 (2014).
31. Yahya, N. A. A., Al-Gaashani, R. & Abd-Shukor, R. Synthesis and characterization of PbO–CdO nanocomposite and its effect on (Bi, Pb)-2223 superconductor. Applied Physics A, 123:**168**, 1-7 (2017).
32. Christuraj, P., Raja, M.D., Pari, S., Kumar, G.S. & Shankar, V.U. Synthesis of Mn doped CdO nanoparticles by co-precipitation method for supercapacitor applications. Materials Today: Proceedings **50** (7), 2679-2682 (2022).
33. Dugan, S., Koç, M.M. & Coşkun, B. Structural, electrical and optical characterization of Mn doped CdO photodiodes. Journal of Molecular Structure 1202 -12017 (2020).
34. Kasirajan, K., Anasthasiya, A.N.A., Aldossary, O.M., Ubaidullah, M. & Karunakaran, M. Structural, morphological, optical and enhanced photodetection activities of CdO films: an effect of Mn doping, Sensors and Actuators, A: Physical **319,** 112531 (2021).

35. Mandal, R. K., Saha, P. & Majumder, T. P. Structural, optical characterization of the synthesized Fe doped CdO Nano particles, its application as a promising photocatalyst for degradation of the hazardous Methyl violet dye. Optik **246**, 167795 (2021).
36. Gudla, U. R., Suryanarayana, B., Raghavendra, V., Parajuli, D., Murali, N., Dominic, S. & Chandramouli, K. Structural, optical and luminescence properties of pure, Fe-doped and glucose-capped CdO Semiconductor nanoparticles for their Antibacterial activity. Journal of Materials Science: Materials in Electronics, **32**(3), 3920-3928 (2021).
37. Menaceur, M., Alleg, S., Abdelouahed, S. & Belghit, R. Structure, Electronic, Magnetic, and Elastic Properties of $Cd_{0.75}TM_{0.25}O$ (TM= Mn, Fe, Co, and Ni) Compounds. Arabian Journal for Science and Engineering, 1-17. (2021).
38. Abbas, S., Basma, H., Al Boukhari J. & Awad, R. Characterization of CdO nanoparticles prepared by co-precipitation method under diferent pH and calcination temperatures. Appl. Phys. A 127: **505,** 1-17 (2021).
39. Leenders, A., Mich, M. & Freyhard, H.C. Influence of thermal cycling on the mechanical properties of VGF melt-textured YBCO. Physica C Supercond. **279,** 173-180 (1997).
40. Gong, J., Wu, J. & Guan, Z. Examination of the indentation size effect in low-load Vickers hardness testing of ceramics. J. Eur. Ceram. Soc. **19**, 2625–2631 (1999).
41. Ling, H.C. & Yan, M.F. Microhardness measurements on dopant modified superconducting $YBa_2Cu_3O_7$ ceramics, J. Appl. Phys. **64,** 130 (1988).
42. Tarkanian, M.L., Neumann, J.P. & Raymond, L. in The Science of Hardness Testing and Its Research Application. ed. By J.H. Westbook, H. Conrad (American Society for Metals, Metal Park, 1973).
43. Weiss, H.J. On deriving Vickers hardness from penetration depth. Phys. Status Solidi **99**, 491 (1987).
44. Li, H. & Bradt, R.C. The microhardness indentation load/size effect in rutile and cassiterite single crystals. J. Mater. Sci. **28**, 917–926 (1993).
45. Hays, C. & Kendall, EG. An analysis of Knoop microhardness. Metallography **6**(4), 275–282 (1973).
46. Li, H. & Bradt, RC. The effect of indentation-induced cracking on the apparent microhardness. J Mater Sci. **31** (4), 1065–1070 (1996).
47. Cabassi, R., Delmonte, D., Abbas, M. M., Abdulridha, A. R. & Gilioli, E. The Role of Chemical Substitutions on Bi-2212 Superconductors. Crystals **10,** 462 (2020).
48. Vinu, S., Sarun, P. M., Biju, A., Shabna, R., Guruswamy, P.& Syamaprasad, U. The effect of substitution of Eu on the critical current density and flux pinning properties of (Bi, Pb)-2212 superconductor. Supercond. Sci. Technol. **21**, 045001 (2008).
49. Lutterotti, L., Maud: a Rietveld analysis program designed for the internet and experiment integration. Acta Crysta. A, **56**, 54-54 (2000).
50. Pallian Murikoli, S., Biju, A., Guruswamy, P. & Upendran, S. J. Am. Ceram. Soc. **90**, 3138–41 (2007).
51. Bi, K.S., Bagiah, H., Halim, Chen S., Lim S., K. & Kechik, M.A. Effects of rare earth nanoparticles (M= Sm_2O_3, Ho_2O_3, Nd_2O_3) Addition on the microstructure and superconducting transition of

$Bi_{1.6}Pb_{0.4}Sr_2Ca_2Cu_3O_{10}$ Ceramics. Sains Malaysiana, **45**(4), 643-651 (2016).

52. Sun, X., Zhao, X., Wu, W., Fan, X., Li, X.G. & Ku, H.C. Pr-doping effect on the structure and superconductivity of $Bi_2Sr_2Ca_{1-x}Pr_xCu_2O_y$ single crystals Physica C **307**, 7 (1998).
53. Yilmazlar, M., Cetinkara, H.A., Nursoy, M., Ozturk, O. & Terzioglu, C. Thermal expansion and Vickers hardness measurements on $Bi_{1.6}Pb_{0.4}Sr_2Ca_{2-x}Sm_xCu_3O_y$ superconductors. Physica C. **442** (2), 101-107 (2006).
54. Khalil, S.M. Effect of Cd Addition on Superconducting Fluctuations and Mechanical Properties of Bi1. 82Pb0. 36Sr2Ca2Cd x Cu3O y System. Low, J.: Temp. Phys. **143,** 31-44 (2006).
55. Sedky, A. & Al-Battat, W. Effect of Y substitution at Ca site on structural and superconducting properties of Bi: 2212 superconductor. Physica B: Condensed Matter **410**, 227-232 (2013).
56. Mohammed, N.H., Abou-Aly, A.I., Ibrahim, I.H., Awad, R. & Rekaby, M., Mechanical properties of $(Cu_{0.5}Tl_{0.5})$-1223 added by nano-SnO_2. J. Alloys Compd. **486**, 733-737 (2009).
57. Basma, H., Abbas, S., Labban, W., Awad, R. & Matar, M. Investigation of the structural and electrical properties of CdO/(Bi,Pb)-2212 superconducting phase. physica scripta accepted manuscript (2022).
58. Abbas, S., Basma, H., Awad, R. & Matar, M. Tailoring the superconducting properties of (Bi, Pb)-2212 by addition of $Cd_{0.95}Mn_{0.05}O$ nanoparticles J.: Temp. Phys. accepted manuscript (2022).
59. Abbas, S., Basma, H., Awad, R. & Hassan, M. M.S. Structural and electrical investigations of novel CdFeO/(Bi,Pb)-2212 superconductor composite phase transitions accepted manuscript (2022).
60. Basma, H., Roumié, M. & Awad. R. Ion Beam Analysis and Electric Properties of $GdBa_2Cu_3O_{7-\delta}$ Added with Nanosized Ferrites $ZnFe_2O_4$ and $CoFe_2O_4$. Mater. sci. appl. **6**(09), 828–840 (2015).
61. Prabitha, V. G., Biju, A., Abhilash Kumar, R. G., Sarun, P. M., Aloysius, R. P. & U. Syamaprasad. Effect of Sm addition on (Bi,Pb)-2212 superconductor. Physica C: Superconduct **433,** 28–36 (2005).
62. Rahal, H. T., Awad, R., Abdel-Gaber, A. M., Marhaba, S. & Abou-Aly, A. I. A comparative study on the influence of the addition of different nano-oxide particles on the thermopower of (Bi, Pb)-2223 superconductor. Appl. Phys. A **125** 365 (2019).
63. Roumié, M., Abdeen, W., Awad, R., Korek, M., Hassan, I. & Mawassi, R. Excess conductivity analysis of $Bi_{1.8}Pb_{0.4}Sr_2Ca_2Cu_3O_{10+\delta}$ added with Nano-ZnO and Nano-Fe_2O_3. J Low Temp Phys **174,** 45–63 (2014).
64. Laitinen, H.A. & Harris, W.E. Chemical Analysis (McGraw-Hill, 1975) p. 358.
65. Karppinen, M., Fukuoka, A., Niinistö, L. & Yamauchi, H. Determination of oxygen content and metal valences in oxide superconductors by chemical methods. Supercond. Sci. Technol. **9**, 121–135 (1996).
66. Klemm, W., Wehrmeyer, G. & Bade, H. BER BUNSEN PHYS CHEM. **63,** 56–59 (1959).
67. Chen, W.M., Lam, C.C., Geng, J. F., Li, L. Y., Hung, K.C. & Jin, X. A New Calculating Formula of Iodometric Titration For High T_c Superconductors. Physica C: Superconduct **270**, 155–158 (1996).

68. Chen, W.M., Wu, X. S., Geng, J.F., Chen, J., Chen, D.B., Jin, X. & Jiang, S. S. An accurate method of iodometric titration to measure copper valence of high-T_c superconductors J Supercond **10**, 41–44 (1997).

69. Hwang, J., Timusk, T. & Gu, G. D. High-transition-temperature superconductivity in the absence of the magnetic-resonance mode. Nature **427**, 714–717 (2004).

70. Jean, F., Collin, G., Andrieux, M., Blanchard, N.& Marucco, J.F. Oxygen non-stoichiometry, point defects and critical temperature in superconducting oxides $Bi_2Sr_2CaCu_2O_{8+d}$ Physica C **339,** 269–280 (2000).

71. Norman, M.R., Ding, H., Randeria, M., Campuzano, J.C., Yokoya, T., Takeuchi, T., Takahashi T., Mochiku, T., Kadowaki, K., Guptasarma, P. & Hinks, D.G. Destruction of the Fermi surface in underdoped high-T_c superconductors. Nature **392**, 157–160 (1998).

72. Alldredge, J. W., Jinho Lee, McElroy, K., Wang, M., Fujita, K., Kohsaka, Y., Taylor, C., Eisaki, H., Uchida, S., Hirschfeld, P. J. & Davis, J. C. Evolution of the electronic excitation spectrum with strongly diminishing hole density in superconducting $Bi_2Sr_2CaCu_2O_{8+\delta}$. Nature Phys **4**, 319–326 (2008).

73. Roesera, H. P., Hetfleischa, F., Huberb, F.M., von Schoenermarka, M. F., Steppera, M., Moritza, A. & Nikoghosyanc, A.S. A link between critical transition temperature and the structure of superconducting $YBa_2Cu_3O_{7-\delta}$, Acta Astronaut. **63**, 1372 (2008).

74. Konsin, P.& Sorkin, B. Dependences of the chemical potential shift and superconducting transition temperature on the hole concentration in $La_{2-x}Sr_xCuO_4$ and $Bi_2Sr_2Ca_{1-x}Y_xCu_2O_{8+delta}$. Supercond. Sci. Technol. **13**, 301-306 (2000).

75. Alcock, C.B. & Li, B. Thermodynamic study of the Cu-Sr-O system. J. Am. Ceram. Soc. **73** (5), 1176-1180 (1990).

76. Stojanovic, E., Biljana, D., Skorokhod, V.V. & Nikolic, M. Advanced Science and Technology of Sintering, Springer Science & Business Media, (2011), doi:10.1007/978-1-4419-8666-5.

77. Broido, A. Sensitive Graphical Method of Treating Thermogravimetric Analysis Data. J. Polym. Sci. Part A- **7**, 1761-1773 (1969).

78. Strobel, P., Capponi, J.J., Marezio, M. & Monod, P. High-temperature oxygen defect equilibrium in superconducting oxide $YBa_2Cu_3O_{7-x}$. Solid State Comm **64,**513-515 (1987).

79. Thesis María Dolores Vázquez-Navarro, A thermogravimetric study of oxygen diffusion in $YBa_2Cu_3O_{7-\delta}$, Ph.D. Thesis, University of Cambridge,1998.

80. Foerster, C.E., Lima, E., Rodrigues Jr, P., Serbena, F.C., Lepienski, C.M., Cantão, M.P., Jurelo A.R. & Obradors, X. Mechanical properties of Ag-doped top-seeded melt-grown YBCO pellets, Braz. J. Phys. **38**, 341-345 (2008).

81. Sahoo, B. & Behera, D. Investigation of superconducting and elastic parameters of YBCO/LSMO thick films, J. Mater. Sci. Mater. Electron. **30**,12992-13004 (2019).

82. Terzioglu, R., Altintas, S.P., Varilci, A. & Terzioğlu, C. Modeling of micro-hardness in the Au doped YBCO bulk superconductors, J. Supercond. Novel Magn. **32**, 3377-3383 (2019).

83. Ozturk, O., Asikuzun, E., Tasci, A.T., Gokcen, T., Ada, H., Koralay, H. & Cavdar, S. Comparison of Vickers microhardness of undoped and Ru doped BSCCO glass ceramic materials, J. Mater.Sci. Mater. Electron. **29**, 3957-3966 (2018).

84. Ma, Q. & Clarke, D.R. Size dependent hardness of silver single crystals. J. Mater. Res. **10**, 853 (1995).

Tables

Table.1 XRD parameters, oxygen content (y), and effective valence of the Cu ions (Cu^{eff}) of (Bi, Pb)-2212 added by nano-CdO, nano-CdMnO, and nano-CdFeO

Table.1										
x	**a (Å)**	**b (Å)**	**c (Å)**	**c/a**	**OD%**	**y**	**Cu^{eff}**		***d***	***z***
0.00	5.416	5.388	30.861	5.698	0.521	8.088	2.238	0.011	51.923	12.111
CdO										
0.01	5.417	5.383	30.845	5.694	0.623	8.113	2.262	0.014	45.900	12.113
0.02	5.418	5.382	30.847	5.693	0.672	8.194	2.343	0.024	35.212	12.115
0.05	5.418	5.378	30.807	5.692	0.631	8.213	2.363	0.026	33.643	12.115
0.10	5.419	5.374	30.844	5.691	0.645	8.273	2.423	0.033	29.831	12.117
CdMnO										
0.01	5.417	5.384	30.842	5.693	0.612	8.172	2.321	0.021	37.339	12.113
0.02	5.417	5.382	30.840	5.693	0.669	8.207	2.337	0.025	34.109	12.113
0.05	5.418	5.381	30.821	5.688	0.818	8.265	2.414	0.032	30.258	12.115
0.10	5.419	5.378	30.804	5.684	0.856	8.308	2.457	0.037	28.144	12.117
CdFeO										
0.01	5.417	5.386	30.839	5.693	0.572	8.142	2.291	0.017	41.019	12.113
0.02	5.419	5.382	30.812	5.686	0.683	8.213	2.361	0.026	33.650	12.117
0.05	5.419	5.381	30.779	5.680	0.701	8.238	2.387	0.029	31.882	12.117
0.10	5.421	5.378	30.772	5.676	0.793	8.331	2.481	0.040	27.197	12.122

Table 2 weight loss (%), weight gain (%) and the activation energies for oxygen diffusion of (Bi, Pb)-2212 added by nano-CdO, nano-CdMnO, and nano-CdFeO with x = 0.00, 0.05 and 0.10 wt.%

Table 2					
x	ΔT (°C)	weight loss (w%)	ΔT (oC)	weight gain (w%)	E (kJ mol^{-1}) (750-890 °C)
0.00	40-568	1.515	568-593	-0.0679	5.508
	750-890	1.6303			
CdO					
0.05	42-568	1.154	568-592	-0.0680	8.080
	750-890	1.6405			
0.10	44-568	2.514	568-592	-0.0682	8.466
	750-890	1.6407			
CdMnO					
0.05	52-570	1.722	568-592	-0.0685	9.798
	750-890	1.6409			
0.10	56-567	2.790	567-592	-0.0687	11.729
	750-890	1.6501			
CdFeO					
0.05	44-570	0.731	570-592	-0.0688	7.007
	750-890	1.6502			
0.10	44-567	1.015	567-592	-0.0689	9.749
	750-890	1.6504			

Table 3 Fitted parameters estimated from several theoretical models for (Bi, Pb)-2212 added by CdO, CdMnO, and CdFeO nanoparticles, with x = 0.00, 0.01, 0.02, 0.05, and 0.10 wt.%

x	Mayer		HK		EPD		PSR		MPSR			IIC	
	n	$A\times10^{-3}$ (N/μm²)	W (N)	$A_1\times10^{-4}$ (N/μm²)	d_o (μm)	$A_2\times10^{-4}$ (N/μm²)	$\alpha\times10^{-2}$ (N/μm)	$\beta\times10^{-4}$ (N/μm²)	α_1 (N)	$\alpha_2\times10^{-3}$ (N/μm)	$\alpha_3\times10^{-4}$ (N/μm²)	m	$K\times10^{4}$ ($N^{(3-5m)/2}$)
0.00	1.406	5.644	0.617	2.654	27.677	2.117	1.725	1.819	0.233	9.830	2.208	0.886	2.071
CdO													
0.01	1.418	5.789	0.582	3.026	24.872	2.427	1.758	2.107	0.256	8.839	2.599	0.891	2.126
0.02	1.449	6.045	0.536	4.001	20.507	3.226	1.880	2.859	0.335	6.182	3.658	0.912	2.444
0.05	1.457	6.755	0.519	4.926	17.997	3.988	2.027	3.555	0.333	6.323	4.538	0.916	2.384
0.10	1.386	5.242	0.707	1.963	35.273	1.553	1.648	1.299	0.163	12.240	1.483	0.880	2.078
CdMnO													
0.01	1.415	6.235	0.624	3.234	24.610	2.605	1.870	2.253	0.159	13.030	2.584	0.894	2.116
0.02	1.468	5.864	0.566	4.262	19.545	3.486	1.906	3.121	0.188	11.880	3.586	0.936	3.116
0.05	1.459	7.356	0.567	5.497	17.291	4.490	2.187	4.002	0.181	13.820	4.605	0.924	2.483
0.10	1.387	5.451	0.726	2.068	34.528	1.641	1.705	1.372	0.107	14.270	1.495	0.880	2.043
CdFeO													
0.01	1.418	6.477	0.600	3.501	23.516	2.806	1.923	2.431	0.238	10.580	2.951	0.894	2.075
0.02	1.476	5.948	0.516	4.681	17.809	3.834	1.895	3.457	0.272	8.025	4.203	0.938	3.095
0.05	1.453	7.797	0.5679	5.748	16.936	4.696	2.246	4.175	0.172	14.470	4.792	0.920	2.323
0.10	1.397	5.685	0.659	2.453	29.636	1.960	1.723	1.669	0.152	12.520	1.908	0.883	2.031

Table 4 Load-independent microhardness parameters in saturation regions were compared using five theoretical models and related mechanical parameters E, Y, K, and B for (Bi, Pb)-2212 added by CdO, CdMnO, and CdFeO nanoparticles with x = 0.00, 0.01, 0.05, and 0.10 wt.%

x	Hv (plateau region)	H_{HKin}	H_{EPDin}	H_{PSRin}	HM_{PSRin}	H_{IICin}	E	Y	K	B
	(GPa)	(GPa)	(GPa)	(GPa)	(GPa)	(GPa)	GPa	GPa	(GPa.μ $m^{1/2}$)	(μ $m^{-1/2}$)
0.00	0.578	0.492	0.393	0.288	0.409	0.577	47.368	0.193	1.278	0.452
CdO										
0.01	0.650	0.561	0.450	0.334	0.482	0.650	53.249	0.217	1.368	0.475
0.02	0.835	0.742	0.598	0.453	0.678	0.833	68.454	0.278	1.604	0.521
0.05	1.025	0.913	0.740	0.563	0.842	1.026	84.020	0.342	1.846	0.555
0.10	0.449	0.364	0.288	0.206	0.275	0.446	36.806	0.150	1.101	0.408
CdMnO										
0.01	0.714	0.600	0.483	0.357	0.479	0.714	58.513	0.238	1.479	0.483
0.02	0.913	0.790	0.646	0.494	0.665	0.911	74.832	0.304	1.689	0.541
0.05	1.180	1.019	0.833	0.634	0.854	1.180	96.690	0.393	2.057	0.574
0.10	0.478	0.383	0.304	0.217	0.277	0.475	39.169	0.159	1.156	0.413
CdFeO										
0.01	0.759	0.649	0.520	0.385	0.547	0.757	62.18	0.253	1.546	0.491
0.02	0.980	0.868	0.711	0.548	0.779	0.977	80.29	0.327	1.744	0.562
0.05	1.236	1.066	0.871	0.661	0.889	1.238	101.29	0.412	2.133	0.579
0.10	0.548	0.455	0.363	0.264	0.354	0.547	44.91	0.183	1.244	0.440

Figures

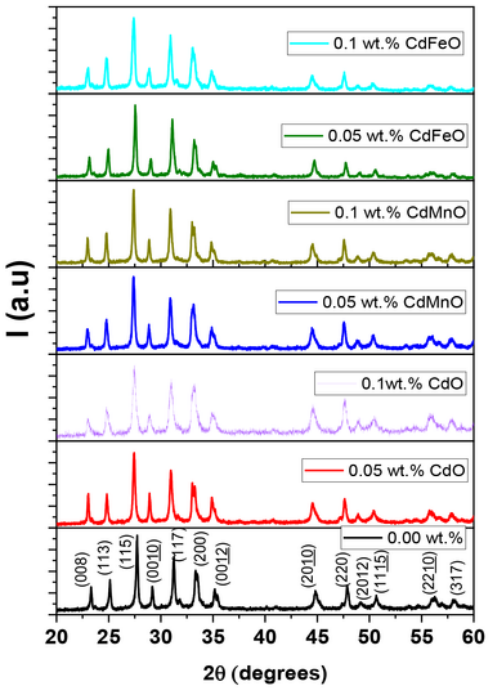

Fig.1-a

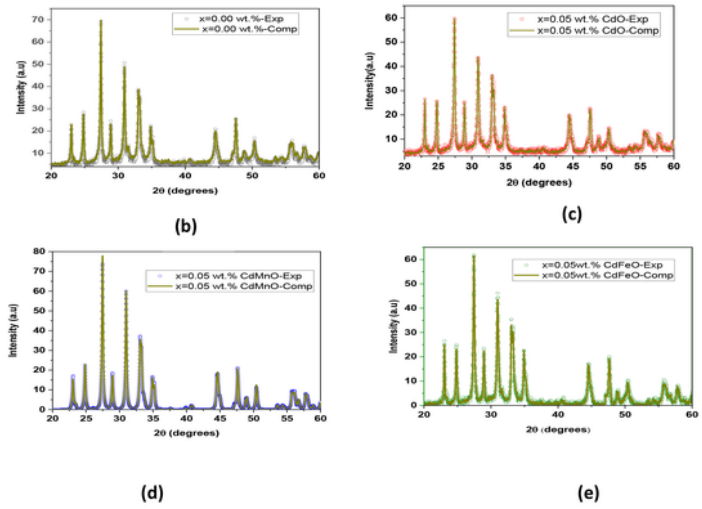

Figs. 1-b to 1-e

Figure 1

a. XRD patterns of (Bi, Pb)-2212 superconducting phase added by nano-CdO, nano- CdMnO, and nano-CdFeO for selected concentrations with x = 0.00, 0.05, and 0.1 wt%.

b to e. Reitveld Refinements of the XRD spectra of selected samples.

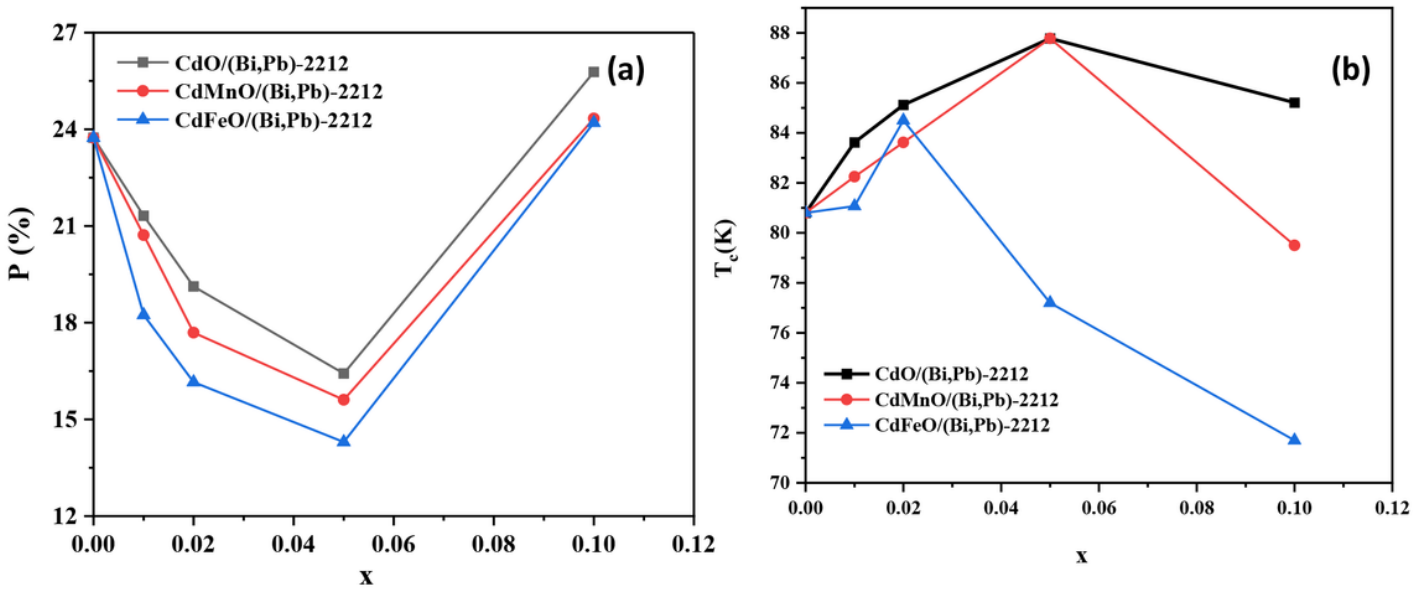

Fig.2

Figure 2

Variation of porosity percentage (P %) (a) and T_c (b) with x.

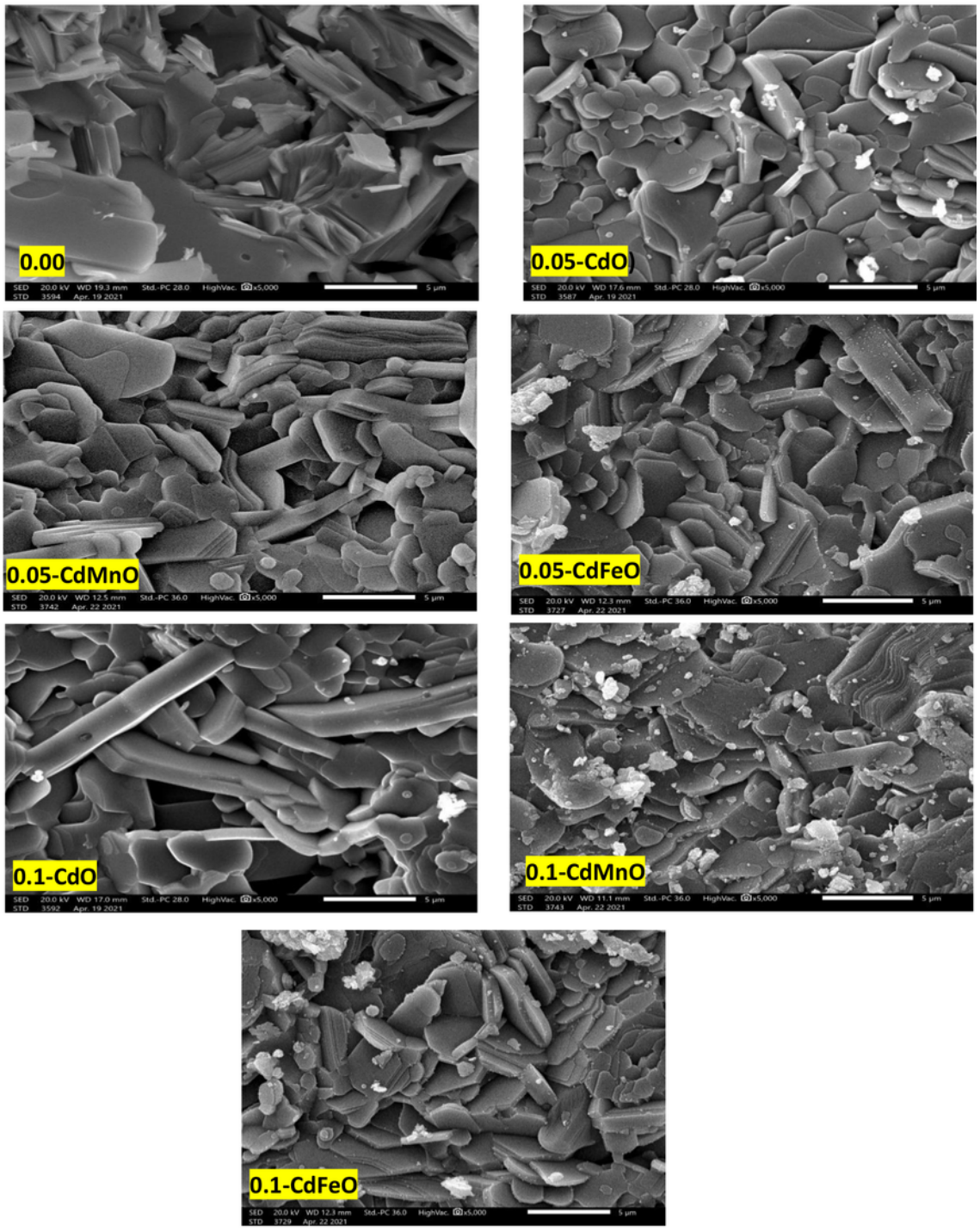

Fig. 3

Figure 3

SEM images for (Bi,Pb)-2212 added with nano-CdO, nano-CdMnO and CdFeO with

x = 0.00, 0.05 and 0.10 wt.%

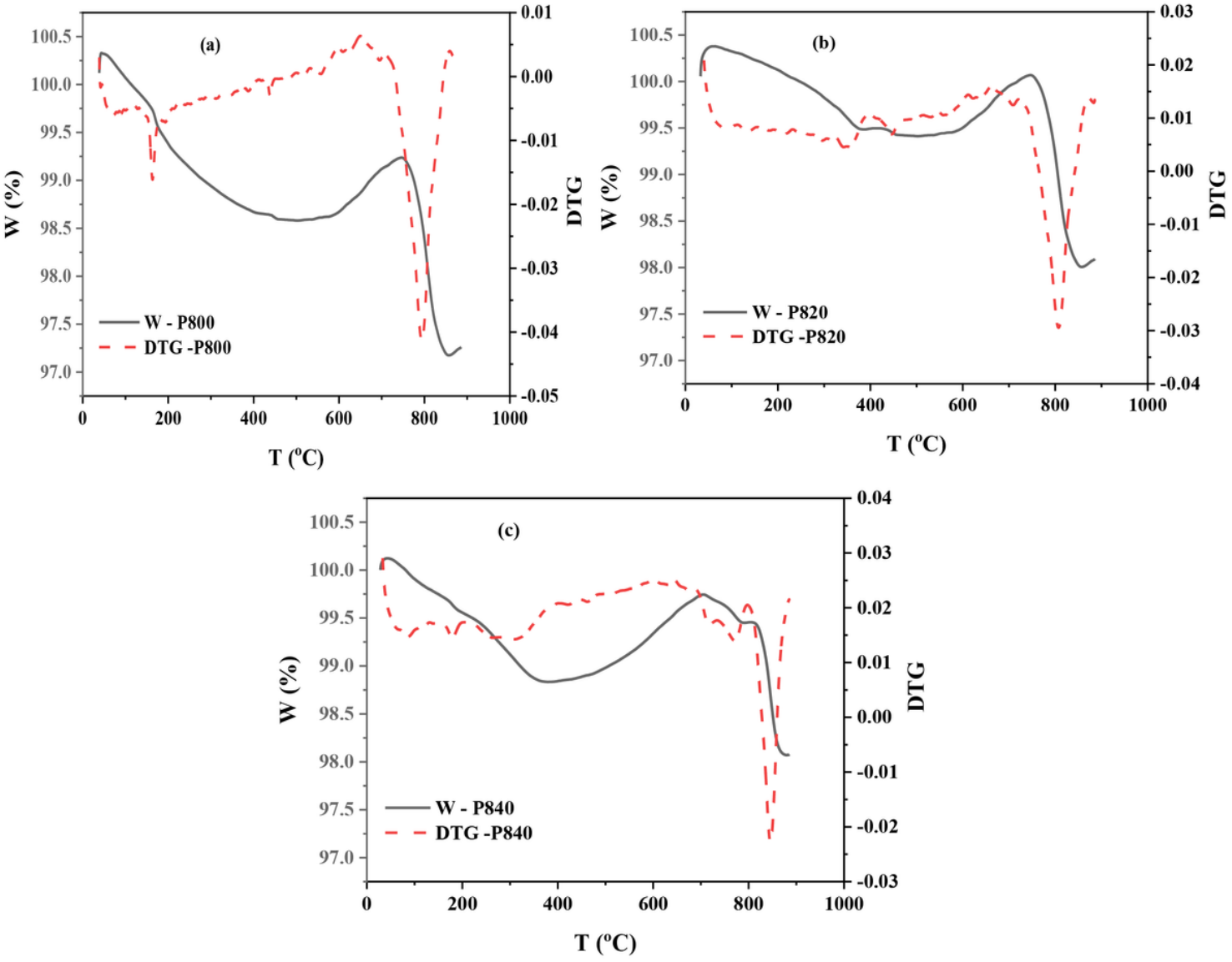

Fig.4

Figure 4

TG–DTA curves of the pure sample at calcination temperatures (a)800 °C (b)820 °C and (c)840°C.

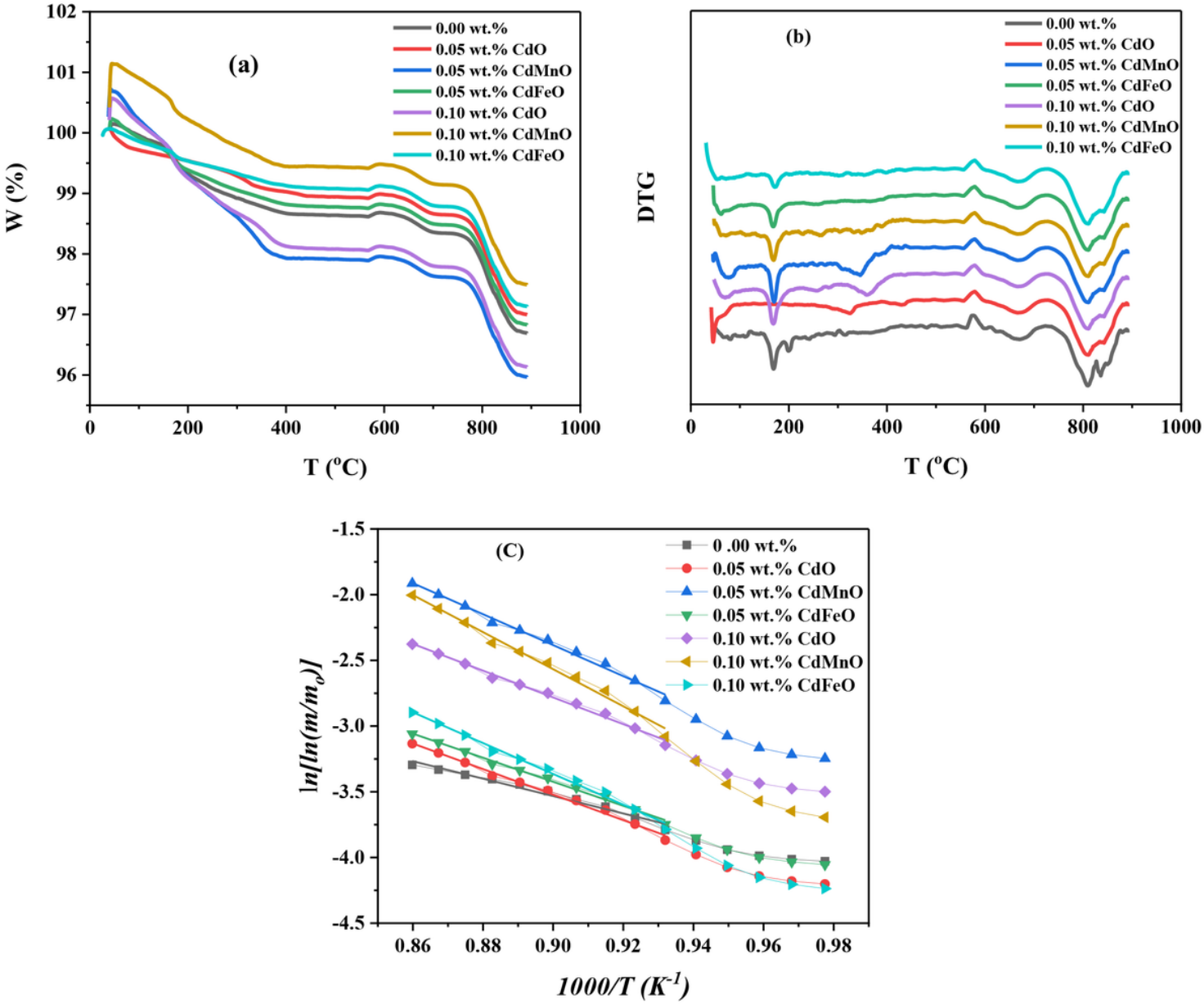

Fig.5

Figure 5

(a) TGA and (b) DTG and (C) ln[lnm/m_o] Vs 1000/T of (Bi,Pb)-2212 added by nano-CdO, nano-CdMnO and nano-CdFeO with x = 0.05 and 0.10 wt.%

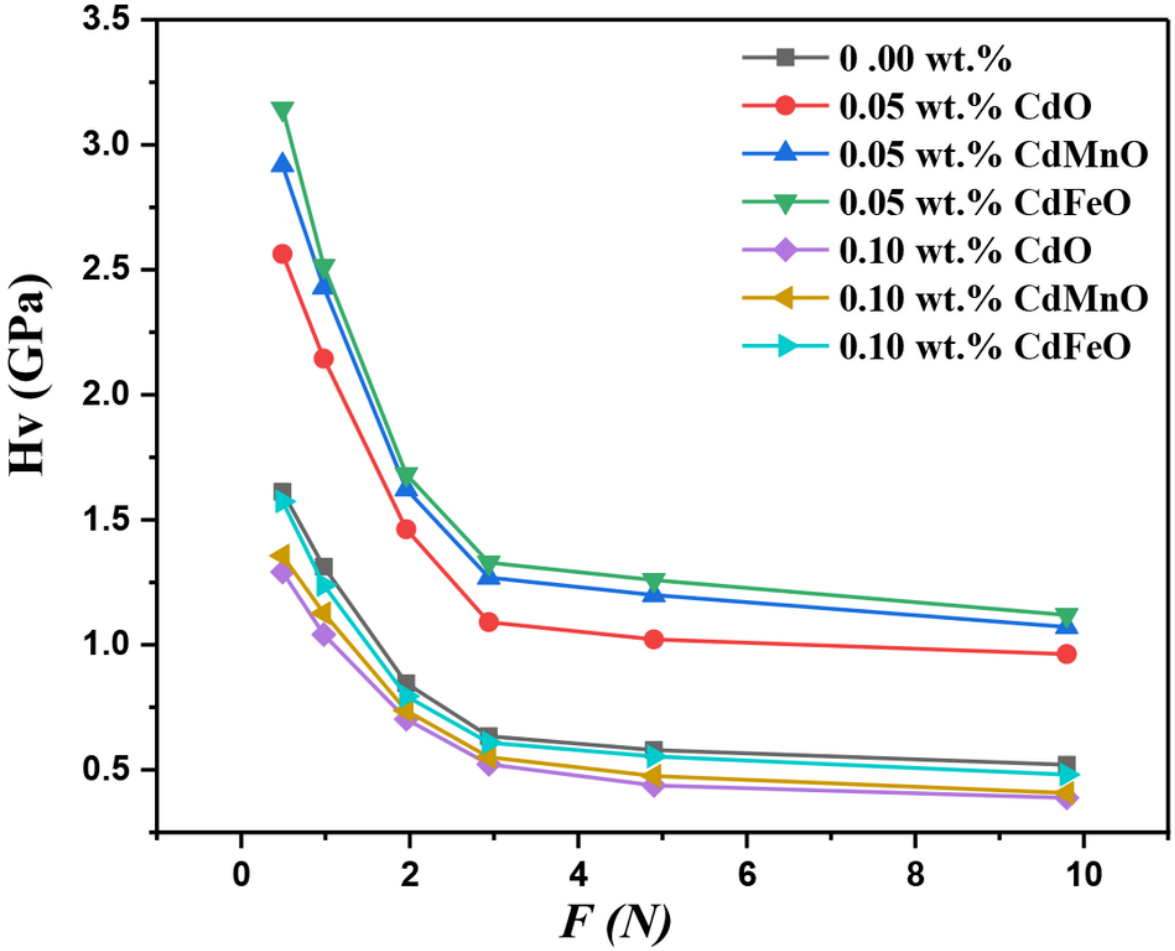

Fig.6

Figure 6

H_V against applied static load F for the (Bi,Pb)-2212 phase added by nano-CdO, nano- CdMnO and nano-CdFeO, x =0.00, 0.05 and 0.10 wt.%.

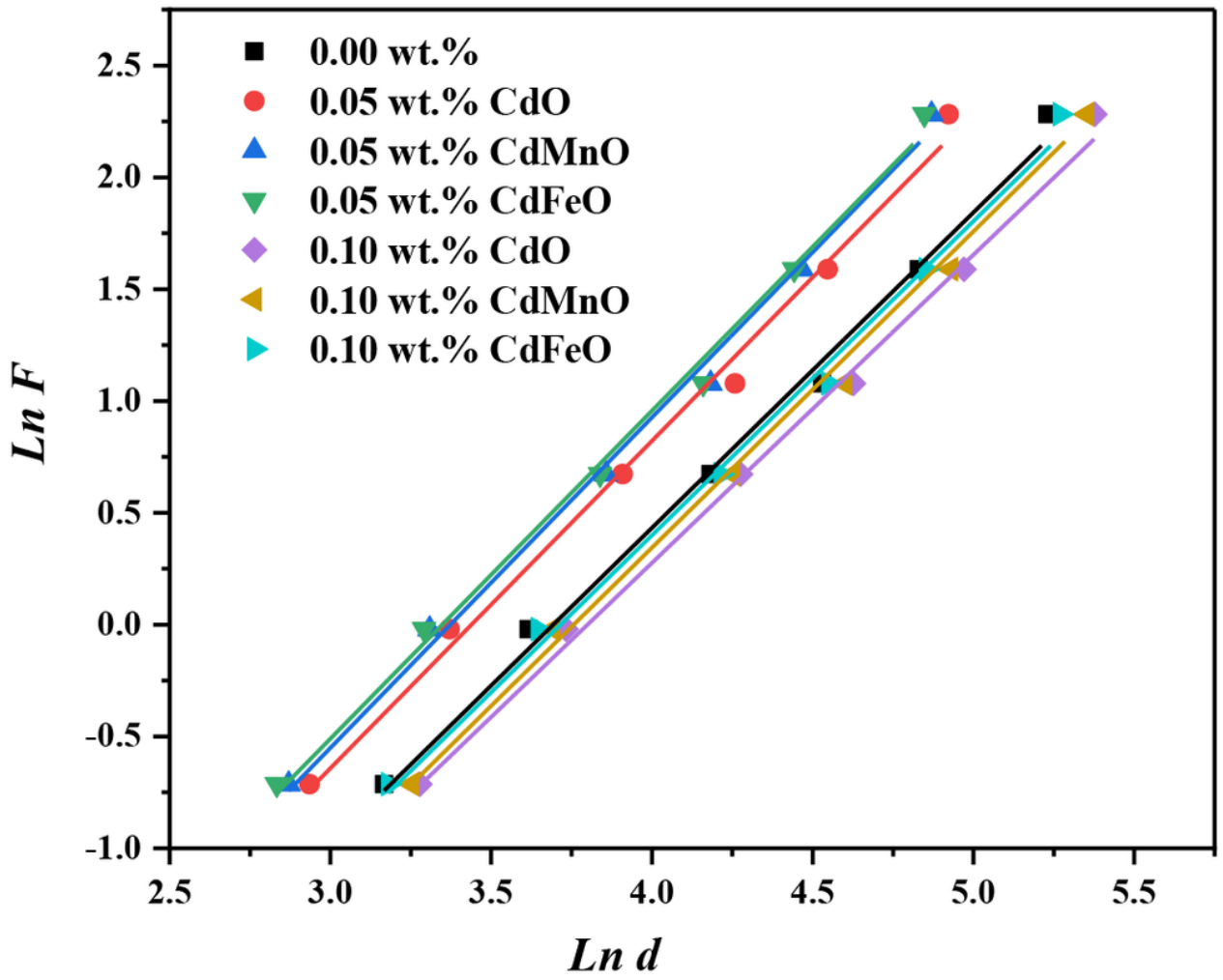

Fig. 7

Figure 7

ln *F* vs ln *d* for the (Bi,Pb)-2212 phase added by nano-CdO, nano-CdMnO and nano-CdFeO, x =0.00, 0.05 and 0.10 wt.%.

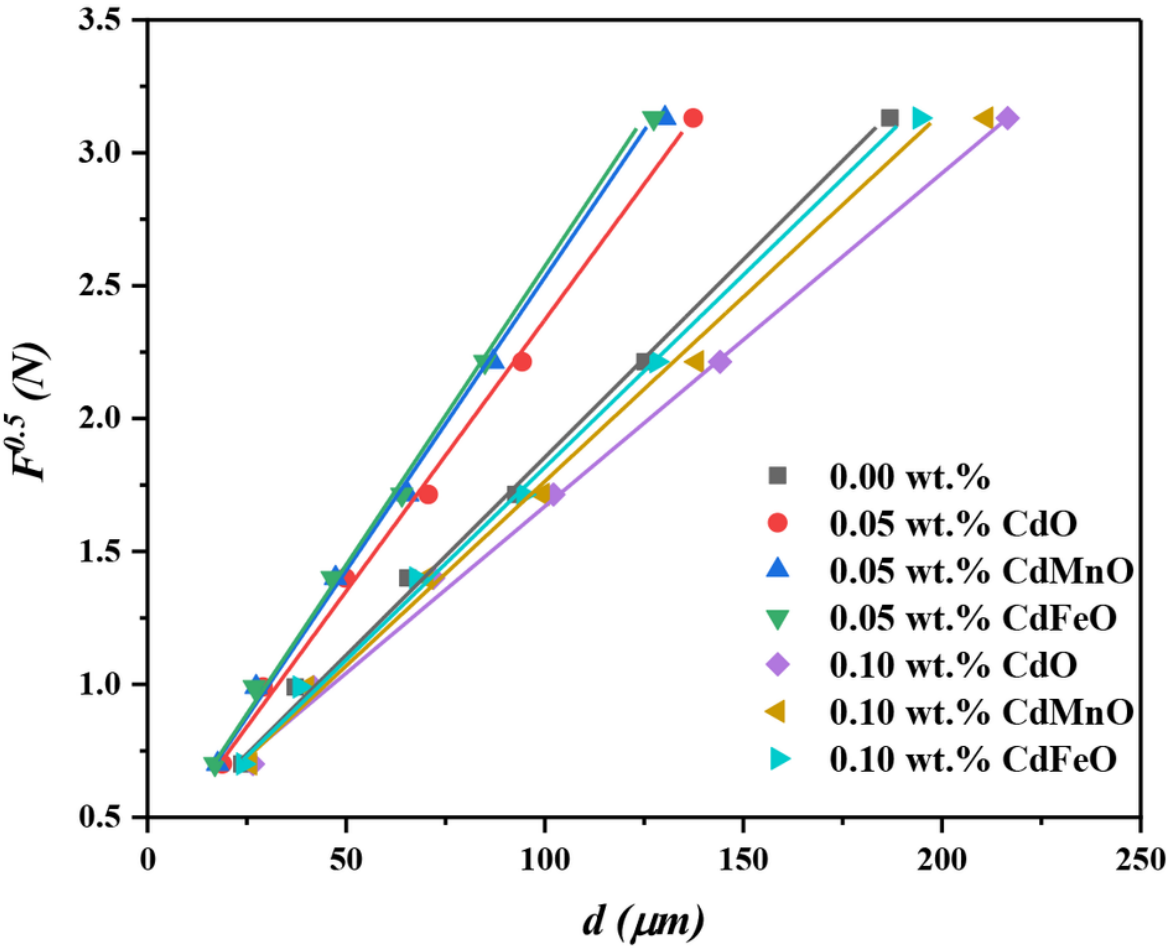

Fig. 8

Figure 8

variation of $F^{0.5}$ against d for the (Bi,Pb)-2212 phase added by nano-CdO, nano-CdMnO and nano-CdFeO, x =0.00, 0.05 and 0.10 wt.%.

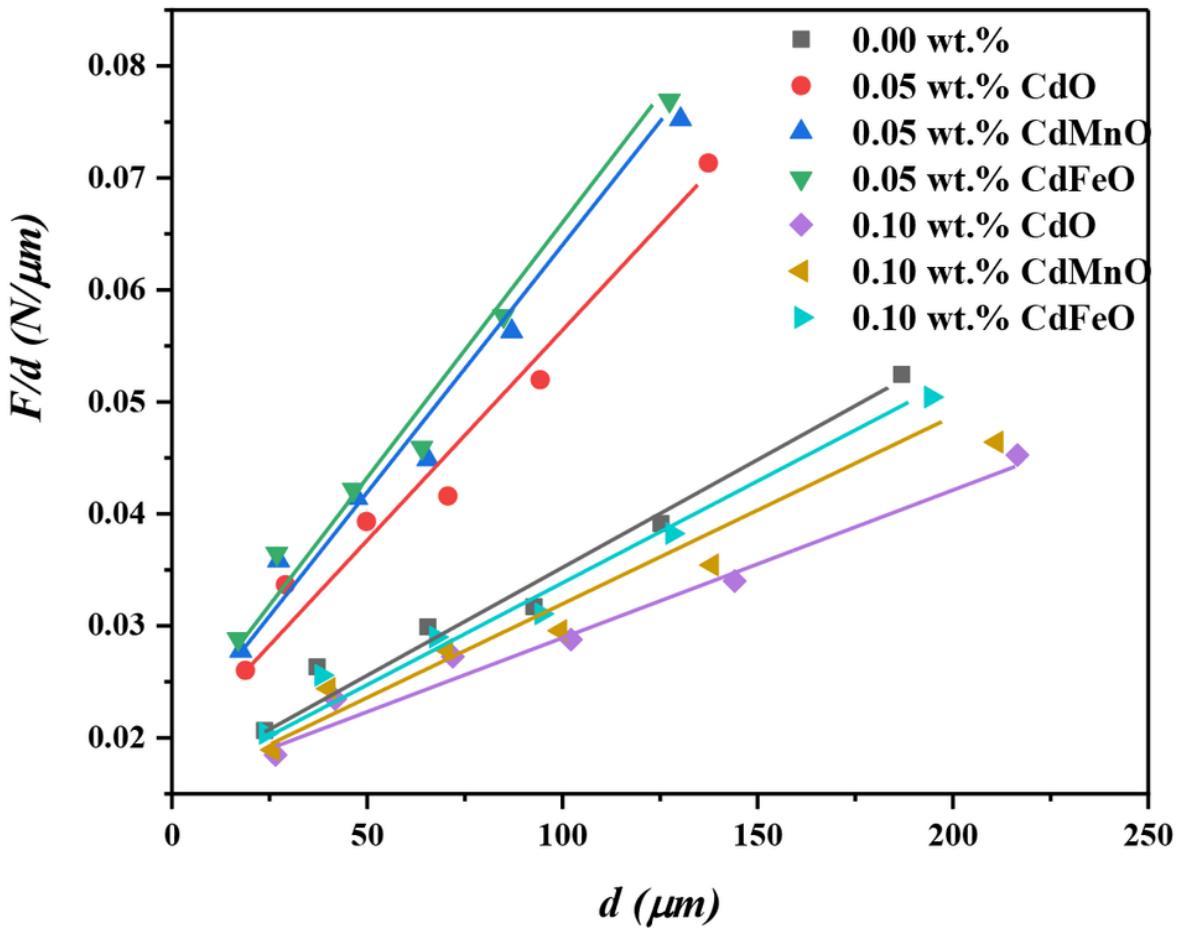

Fig. 9

Figure 9

F/ *d* versus *d* for the (Bi,Pb)-2212, added by CdO, CdMnO and CdFeO nanoparticles, with x =0.00, 0.05 and 0.10 wt.%.

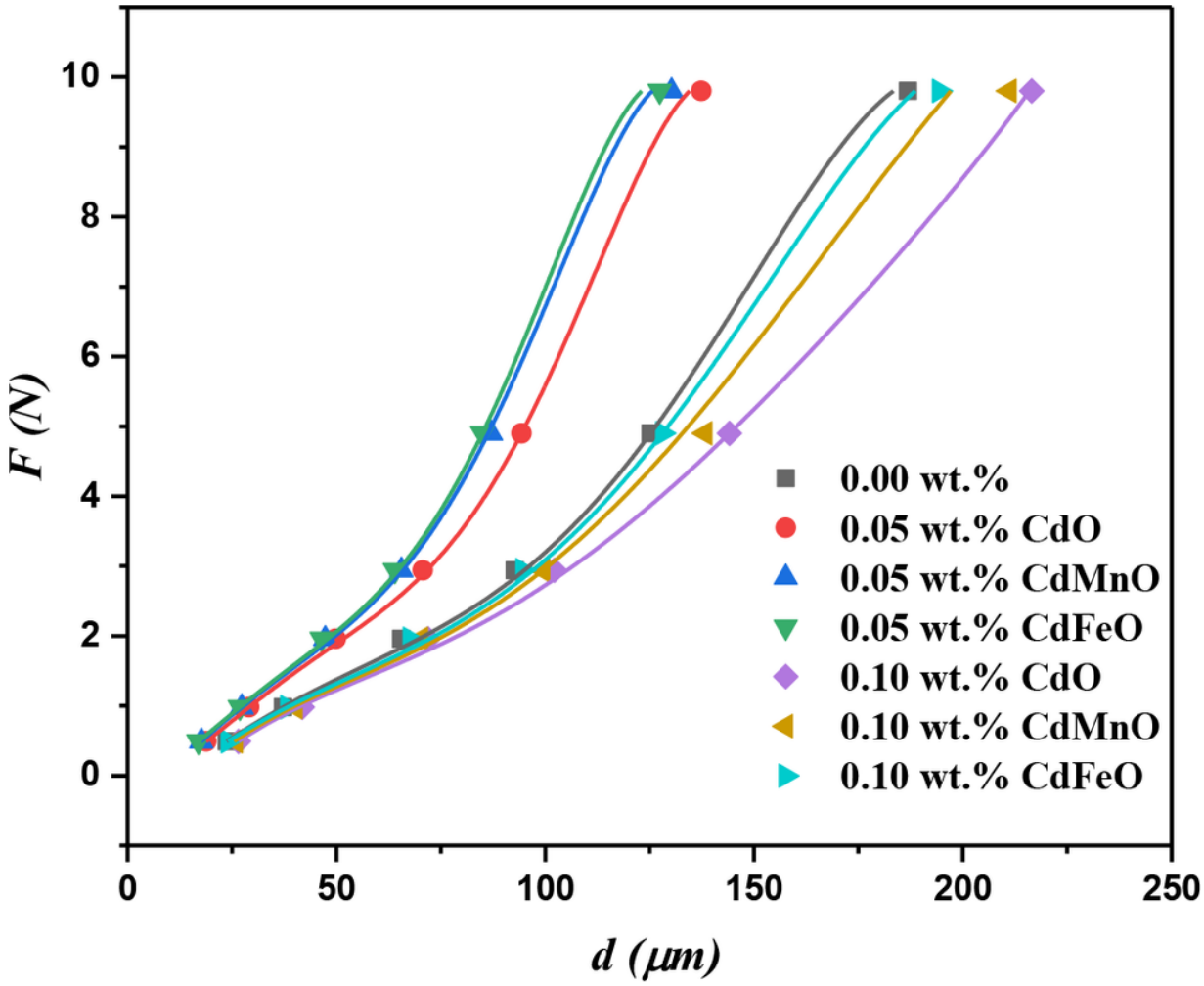

Fig. 10

Figure 10

Variations of *F* against *d* for the (Bi,Pb)-2212, added by CdO, CdMnO and CdFeO nanoparticles, with x =0.00, 0.05 and 0.10 wt.%.

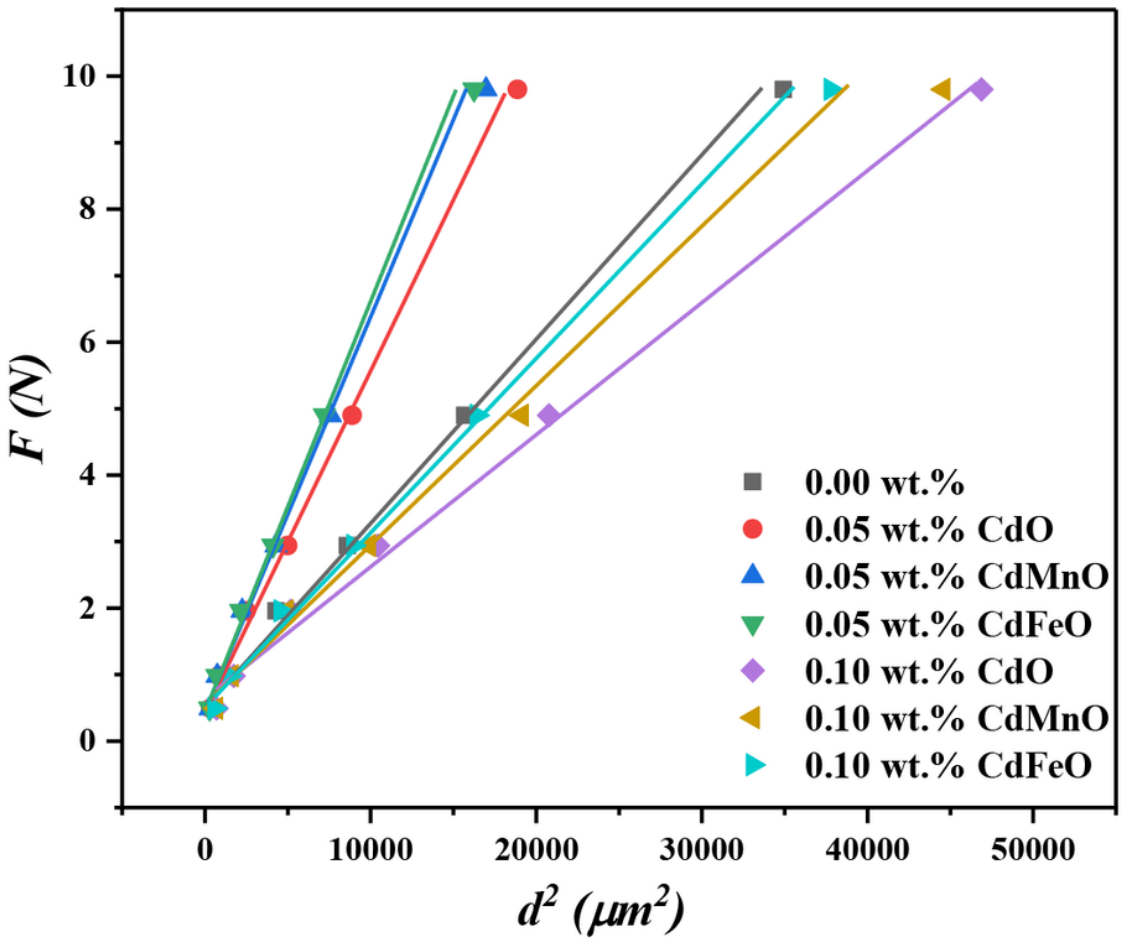

Fig. 11

Figure 11

linear plotting of *F* versus d^2 for the (Bi,Pb)-2212, added by CdO, CdMnO and CdFeO nanoparticles, with x =0.00, 0.05 and 0.10 wt.%.

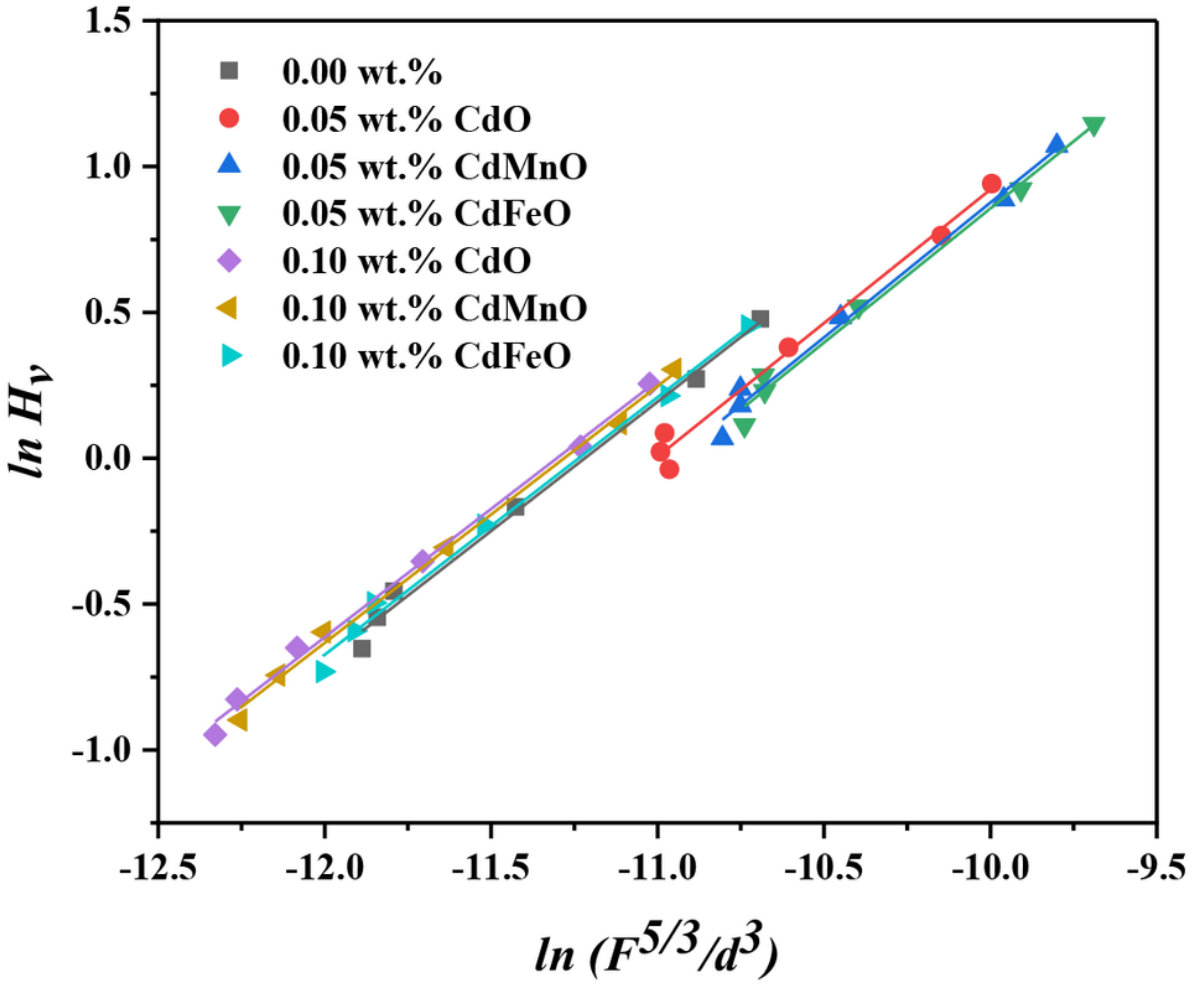

Fig. 12

Figure 12

Variation of Ln (*Hv*) with Ln ($F^{5/3}/d^3$) according to IIC model for the (Bi,Pb)-2212, added by CdO, CdMnO and CdFeO nanoparticles, with x =0.00, 0.05 and 0.10 wt.%.